Mechanisms of along-channel sediment transport in the North Passage of the Yangtze Estuary and their response to large-scale interventions

Chenjuan Jiang · Huib E. de Swart · Jiufa Li · Gaofeng Liu

Abstract The effects of large-scale interventions in the North Passage of the Yangtze Estuary (the Deep Waterway Project, DWP) on the along-channel flow structure, suspended sediment distribution and its transport along the main channel of this passage are investigated. The focus is explaining the changes in net sediment transport in terms of physical mechanisms. For this, data of flow and suspended sediment concentration (SSC), which were collected simultaneously at several locations and at different depths along the main channel of the North Passage prior to and after the engineering works, were harmonically analyzed to assess the relative importance of the transport components related to residual (time-mean) flow and various tidal pumping mechanisms. Expressions for main residual flow components were derived using theoretical principles. The SSC revealed that the estuarine turbidity maximum (ETM) was intensified due to the interventions, especially in wet seasons, and an upstream shift and extension of the ETM zone occurred. The amplitude of the M_2 tidal current considerably increased, and the residual flow structure was significantly altered by engineering works. Prior to the DWP, the residual flow structure was that of a gravitational circulation in both seasons, while after the DWP, there was seaward flow throughout the channel during the wet season. The analysis of net sediment transport reveals that during wet seasons and prior to the DWP, the sediment trapping was due to asymmetric tidal mixing, gravitational circulation, tidal rectification, and M_2 tidal pumping, while after the DWP, the trapping was primarily due to seaward transport caused by Stokes return flow and fresh water discharge and landward transport due to M_2 tidal pumping and asymmetric tidal mixing. During dry seasons, prior to the DWP, trapping of sediment at the bottom relied on landward transports due to Stokes transport, M_4 tidal pumping, asymmetric tidal mixing, and gravitational circulation, while after the DWP the sediment trapping was caused by M_2 tidal pumping, Stokes transport, asymmetric tidal mixing, tidal rectification, and gravitational circulation.

C. Jiang · J. Li (✉)
State Key Laboratory of Estuarine and Coastal Research,
East China Normal University, 3663 Zhongshan Rd. N.,
200062 Shanghai, China
e-mail: jfli@re.ecnu.edu.cn

C. Jiang · H. E. de Swart
Institute for Marine and Atmospheric Research Utrecht,
Utrecht University, Princetonplein 5, 3584 CC,
Utrecht, the Netherlands

G. Liu
Shanghai Estuarine & Coastal Science Research Center,
1045 Xingsheng Rd,
201201 Shanghai, China

1 Introduction

In many estuaries, the joint action of tidal currents and residual (time-mean) currents causes entrainment, transport, and settling of fine sediments. The resulting along-channel distribution of mean suspended sediment concentration (SSC) is often characterized by a turbidity maximum, i.e., a location where the concentration of suspended sediment attains a maximum, hence where the suspended sediment is trapped. Thus, a zone of sediment accumulation may form, causing navigational problems that consequently require dredging, as well as

ecological problems, such as oxygen deficits (cf. Cloern and Jassby 2012, and references herein).

Such a situation actually occurs in the Yangtze Estuary, located at the east coast of mainland China. Here, a large-scale mouth-bar area is present (Fig. 1). One of four channels that intersect this bar is the North Passage, which has minimum depths that are less than 6.5 m in the main channel. To improve navigability of the major channel toward Shanghai Harbor, a large-scale Deep Waterway Project (DWP) was carried out during the period 1998 until 2011. The main engineering works included two wide spacing training walls, 19 long groins, diversion works, and jetties. These constructions were completed in 2004, while after that, the deepening of the waterway relied on local lengthening of groins and dredging. The waterway was deepened to 8.5 m (June 2001), 10 m (March 2005), and finally to 12.5 m (May 2011). To maintain the water depth, the annual dredging rates were around 20, 40, and 70 million tons, respectively. The quantity of dredging was significantly larger than 25 million tons per year that engineers originally anticipated. Since the third phase of the project started, the dredging has taken place continuously and caused a persistent background SSC. The along-channel distribution of the siltation corresponded to the distribution of suspended sediment, and most siltation occurred in the core area of turbidity maximum (Shanghai Waterway Engineering Design and Consulting Co., Ltd. 2011). Thus, clear understanding of mechanisms

that affect along-channel residual sediment transport and its response to the interventions is required to help decreasing siltation in the waterway and to improve decision strategies for estuarine management.

Along-channel residual sediment transport in tidal estuaries is mainly driven by residual currents, tidal asymmetries, and sediment processes associated with the settling, erosion, and flocculation of sediment (Officer 1981; Dyer 1997; Winterwerp 2002). Residual flows in the along-channel direction can be generated by river discharge, horizontal density gradients due to salinity and turbidity gradients (Hansen and Rattray 1965; Festa and Hansen 1978; Talke et al. 2009), wind drag on the sea surface (North et al. 2004), tidal rectification (Huijts et al. 2009), and by asymmetries in stratification and mixing (Stacey et al. 2008; Burchard and Hetland 2010; Cheng et al. 2011). Besides residual sediment transport due to residual currents, tidal pumping mechanisms related to correlations between tidal currents and SSC were considered to be significant in sediment trapping (Dyer 1997; Li and Zhang 1998). Tidal pumping mechanisms investigated include transport by spatial settling lag (Postma 1967) and by combined tidal asymmetry and settling lag (Groen 1967; Jay and Musiak 1994; Schuttelaars and de Swart 1996; Chernetsky et al. 2010).

Dyer (1988, 1997) introduced a method to decompose observed residual sediment transport into several terms, involving transport by Eulerian residual flow, Stokes transport,
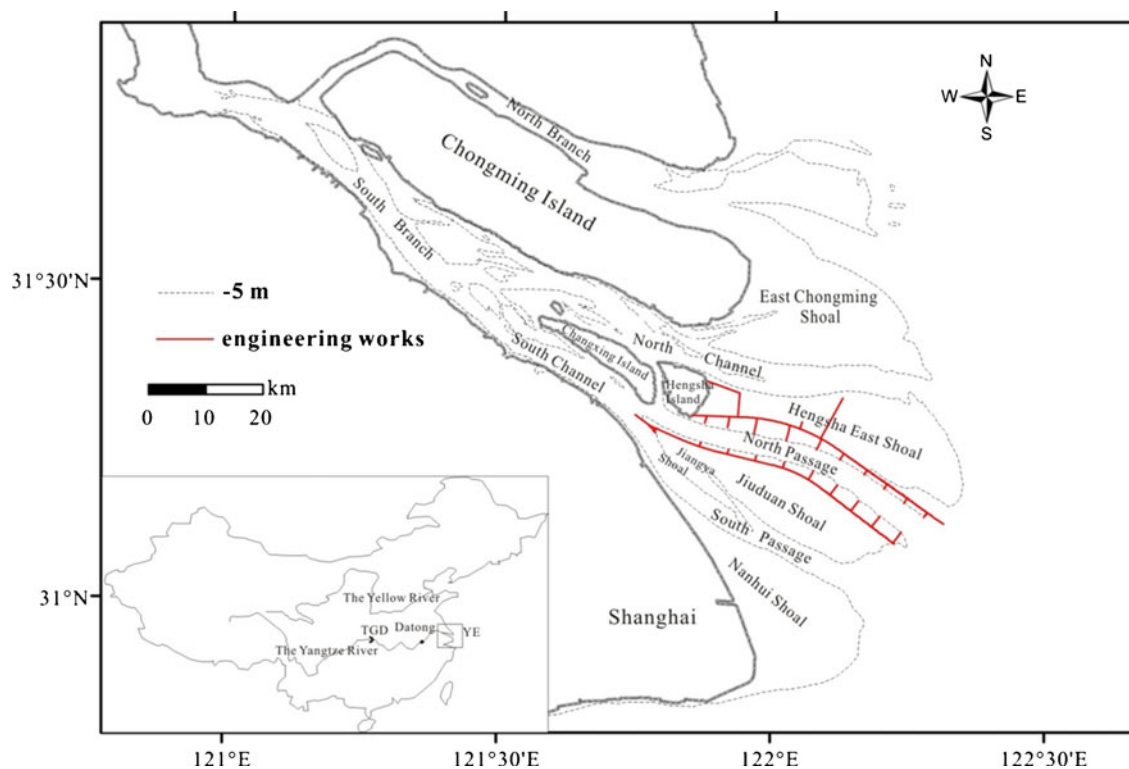

Fig. 1 Map of the lower Yangtze Estuary. The *red solid lines* indicate the training walls, groins, and jetties constructed in the Deep Waterway Project

and tidal pumping. This method has been applied to several estuaries to identify mechanisms causing net sediment transport (Dyer 1988; Uncles et al. 1984, 1985). It was also applied to the Yangtze Estuary by Li and Zhang (1998) using field data surveyed in 1988. They showed that net sediment transport in the North Passage was mainly dominated by a seaward contribution due to residual flow and two landward contributions due to tidal pumping and Stokes transport. Liu et al. (2011) identified the importance of the landward residual flow in the bottom layer in sediment trapping by analyzing data surveyed in a dry season in the end phase of the DWP (January 2008). However, no identification of the roles of different tidal components was presented, nor that of residual flows forced by different agents. Besides, variation in the mechanisms of along-channel sediment transport prior to and after the interventions in the North Passage is still an open problem.

The purpose of this paper is to identify the effects of the DWP (engineering works and the continuous maintenance dredging) on the flow structure, suspended sediment distribution, and its net transport (i.e., tidal averaged transport) along the main channel of the North Passage, with focus on explaining the changes in net sediment transport in terms of physical mechanisms. A new approach, based on combining harmonic analysis of field data and theoretical results of an analytical model, will be used to assess flow and net sediment transport due to individual mechanisms. In Section 2, the details on the field measurements are presented, followed by a description of the method of harmonic analysis on water height, velocity, and SSC data, as well as computation of net sediment fluxes and transports due to individual harmonic components. Also, the analytical model to derive the main residual flow components is presented here. In Section 3, the results of tidal and seasonal variation of SSC prior to and after DWP are presented, focusing on the changes in the strength and location of the ETM. This is followed by showing the harmonic components of the flow and SSC and the net sediment fluxes, as well as transports that they induce. Also, the physical mechanisms that underlie these transports will be identified. Section 4 contains a discussion and the last section contains the conclusions.

2 Data and methods

2.1 Data

Measurements were carried out simultaneously at several stations in the main channel of the North Passage (Fig. 2) by anchoring a boat at each station. Due to the fact that it is forbidden to perform long-term measurements in the waterway, all the measurement sites were just outside the deep waterway (Fig. 2), either slightly to the north or to the south. Selection of

the sites was based on the criterion that here the strongest tidal current in the cross section, excluding the waterway, occurs.

These measurements, organized by Yangtze Estuary Waterway Administration Bureau, Ministry of Transport of China, were undertaken at spring tides during June 1999, February 2000, August 2008, and February 2009, under calm weather conditions. During these campaigns, data of along-channel currents, salinity, and SSC at difference depths were collected during one to two full tidal cycles. These data were collected at six locations with relative depths of 0 (actually 0.5 m below the water surface), 0.2, 0.4, 0.6, 0.8, and 1 (near bottom) of each station at every hour. The current velocity was measured by direct-reading current meters, and salinity and SSC were obtained by analyzing water samples taken during measurements. The direct-reading current meter is a device that was widely used prior to availability of ADCP (cf. Uncles et al. 2006). The current meter used in the measurements is type SLC9-2, a mechanical current meter with a propeller to measure the velocity of the current and a rudder at the end to control the current meter to be parallel to the direction of current, produced by the Instrument Company of Qingdao Ocean University (now China Ocean University), with an accuracy of $0.01\ \mathrm{ms}^{-1}$.

The detailed information about each survey measurement, involving the exact time, duration, stations, and monthly mean river discharge at the tidal limit, is presented in Table 1. The data of June 1999 and February 2000 were considered to represent the conditions prior to the interventions during the wet and dry season, and the data of August 2008 and February 2009 were considered to represent the conditions after the interventions during the wet and dry season. Hereafter, these four cases are called the wet season prior to the DWP, dry season prior to the DWP, wet season after the DWP, and dry season after the DWP. The difference in river discharge corresponding to the measurements of the same season in different years is 7 % in the wet season and 5 % in the dry season. Thus, the data prior to and after the interventions are comparable.

2.2 Harmonic analysis

To identify the net sediment transport due to different agents, it is convenient to decompose tidal height, velocity, and SSC into their mean components and components related to tides by harmonic analysis. According to the harmonic analysis on the long time tidal height series, the tide in the Yangtze Estuary is dominated by the diurnal tide (O_1, K_1), semi-diurnal tide (M_2), and quarter-diurnal tide (M_4), so these data are decomposed into a mean part and three tidal components. Due to the fact that the differences between tidal frequencies of O_1 and K_1 are small, these two tidal constituents are not separated in the harmonic analysis, and they are represented by a diurnal tidal component with a frequency of $0.7 \times 10^{-4} \mathrm{s}^{-1}$.
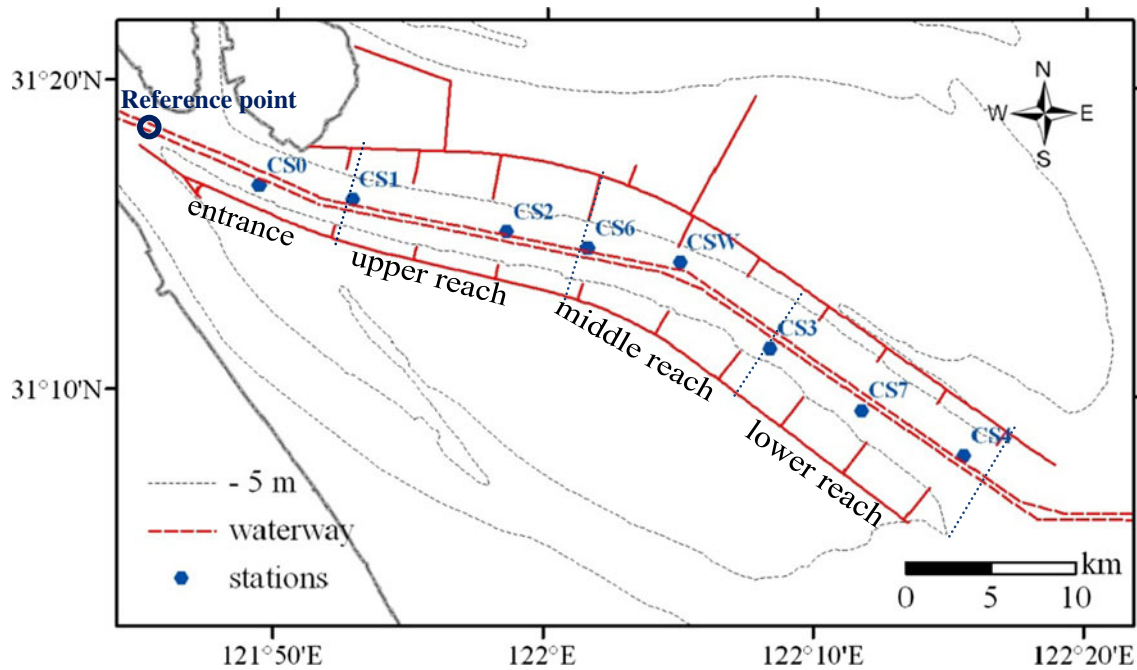
Fig. 2 Locations of the stations where data of flow, salinity, and suspended sediment concentration were collected during tidal cycles in the North Passage. The *blue dotted lines* are the boundaries of different reaches, and the definition of each reach is used for interpretation in the text. The *dark blue circle* is the reference point at the landward boundary of the North Passage

The tidal height data for a given period of time at a certain station is thus represented as a harmonic series

$$h(t) = H + \eta_1 \cos(\sigma_1 t - \psi_1) + \eta_2 \cos(\sigma_2 t - \psi_2) + \eta_3 \cos(\sigma_3 t - \psi_3) \quad (1)$$

Here, h is the measured instantaneous water depth and t is time. Further, H is the mean water depth, and $\sigma_1 \sim 0.7 \times 10^{-4} \text{s}^{-1}$, $\sigma_2 \sim 1.4 \times 10^{-4} \text{s}^{-1}$, and $\sigma_3 \sim 2.8 \times 10^{-4} \text{s}^{-1}$ are the tidal frequencies of the diurnal tide, semi-diurnal tide, and quarter-diurnal tide. Furthermore, η_1, η_2, η_3, and Ψ_1, Ψ_2, Ψ_3 are the amplitudes and phases of diurnal tidal constituent O_1–K_1, semi-diurnal tidal constituent M_2, and quarter-diurnal tidal constituent M_4. The values of these coefficients are determined by minimizing the overall error between observed and modeled $h(t)$.

Data of velocity and SSC at one station are used at six locations with relative depth of 0, 0.2, 0.4, 0.6, 0.8, and 1 at every hour. Thus, flow velocity is decomposed as

$$u(t,j) = U_0(j) + U_1(j) \cos(\sigma_1 t - \varphi_1(j)) + U_2(j) \cos(\sigma_2 t - \varphi_2(j)) + U_3(j) \cos(\sigma_3 t - \varphi_3(j)) \quad (2)$$

Here, j denotes the vertical location of the measurements, equaling 1 to 6 from surface to bottom. Further, u is the measured velocity, U_0 is the residual flow, while U_1, U_2, U_3 and φ_1, φ_2, φ_3 are the amplitudes and phases of diurnal tidal current, semi-diurnal tidal current, and quarter-diurnal tidal current.

Suspended sediment concentration is decomposed as

$$c(t,j) = C_0(j) + C_1(j) \cos(\sigma_1 t - \theta_1(j)) + C_2(j) \cos(\sigma_2 t - \theta_2(j)) + C_3(j) \cos(\sigma_3 t - \theta_3(j)) \quad (3)$$

In this expression, c is the measured SSC and C_0 is the tidal averaged concentration, which includes the contribution from sediment input from the river and sediment resuspension due to residual flow, tide, wave action, and dredging. Furthermore,

Table 1 Detailed information on survey measurements

Month/year	Observation period (date/h)	Duration (h)	Observation stations	Monthly mean river discharge at tidal limit (m³ s⁻¹)
June 1999	29/20:00–30/9:00	14	CS1, CS2, CS3, CS4	42,000
February 2000	21/22:00–22/22:00	25	CS1, CS2, CS3, CS4	12,300
August 2008	1/18:00–2/22:00	29	CS0, CS1, CS2, CS6, CSW, CS3, CS7	39,064
February 2009	9/17:00–10/22:00	30	CS0, CS1, CS2, CS6, CSW, CS3, CS7, CS4	11,715

C_1, C_2, C_3 and θ_1, θ_2, θ_3 are the amplitudes and phases of concentration related to diurnal tide, semi-diurnal tide, and quarter-diurnal tide, respectively.

Next, the local net sediment flux $F(j)$ due to residual flow and various tidal pumping mechanisms is considered. From Eqs. 2 and 3, it follows

$$F(j) = \overline{u(j,t)c(j,t)} = \underbrace{U_0(j)C_0(j)}_{F_0} + \underbrace{U_1(j)C_1(j)\cos(\varphi_1(j) - \theta_1(j))/2}_{F_{O1,K1}}$$
$$+ \underbrace{U_2(j)C_2(j)\cos(\varphi_2(j) - \theta_2(j))/2}_{F_{M2}} + \underbrace{U_3(j)C_3(j)\cos(\varphi_3(j) - \theta_3(j))/2}_{F_{M4}} \quad (4)$$

Here, the overbar $\overline{\cdot}$ denotes averaging over a tidal period, F_0 is the net sediment flux due to residual flow, and $F_{O1,K1}$, F_{M2}, F_{M4} are net fluxes related to the diurnal tide O_1–K_1, semi-diurnal tide M_2, and quarter-diurnal tide M_4. Longitudinal–vertical structure of net sediment flux due to individual forcing agents was obtained by interpolating sediment fluxes at different locations. The spatial interpolation was done in Matlab with a cubic spline interpolation method. Additional analysis of the August 2008 data was performed, in which we used a different interpolation scheme (cubic). The relative error between these data was found them to be small (less than 1 %).

Finally, the net sediment transport per unit width was computed, which is the tidal average of the vertical integration of the sediment flux. Due to the fact that data are available at only six locations of a vertical water column, it is assumed that the water column can be divided into six layers and the observed velocity and SSC at a certain relative depth represent the average condition of the layer in which it locates. So, the net sediment transport per unit width is the discrete integration of the sediment fluxes at the six relative depths:

$$T = \sum_{j=1}^{6} \overline{u(j,t)c(j,t)h(t)p(j)} = \underbrace{\sum_{j=1}^{6} F_0(j)p(j)H}_{T_0}$$

$$+ \underbrace{\sum_{j=1}^{6} F_{O1,K1}(j)p(j)H}_{T_{O1,K1}} + \underbrace{\sum_{j=1}^{6} F_{M2}(j)p(j)H}_{T_{M2}} + \underbrace{\sum_{j=1}^{6} F_{M4}(j)p(j)H}_{T_{M4}}$$

$$+ \underbrace{\sum_{i=1}^{3}\sum_{j=1}^{6} U_i(j)\eta_i(j)\cos(\varphi_i(j) - \psi_i(j))C_0(j)p(j)/2}_{T_{\eta u C_0}}$$

$$+ \underbrace{\sum_{i=1}^{3}\sum_{j=1}^{6} C_i(j)\eta_i(j)\cos(\theta_i(j) - \psi_i(j))U_0(j)p(j)/2}_{T_{\eta c U_0}} + T_{\eta c u}, \quad (5)$$

where

$$T_{\eta c u} = \sum_{j=1}^{6} U_1(j)\eta_2(j)C_1(j)\cos(\varphi_1(j) - \psi_2(j) + \theta_1(j))p(j)/4$$
$$+ \sum_{j=1}^{6} U_2(j)\eta_1(j)C_1(j)\cos(\varphi_2(j) - \psi_1(j) - \theta_1(j))p(j)/4$$
$$+ \sum_{j=1}^{6} U_1(j)\eta_1(j)C_2(j)\cos(\varphi_1(j) + \psi_1(j) - \theta_2(j))p(j)/4$$
$$+ \sum_{j=1}^{6} U_3(j)\eta_2(j)C_2(j)\cos(\varphi_3(j) - \psi_2(j) - \theta_2(j))p(j)/4$$
$$+ \sum_{j=1}^{6} U_2(j)\eta_2(j)C_3(j)\cos(\varphi_2(j) + \psi_2(j) - \theta_3(j))p(j)/4$$

Here, the upper bar denotes a tidal-average or mean. Further, j denotes layers, and $p(j)$ is the relative thickness of the layer, which is 0.1, 0.2, 0.2, 0.2, 0.2, and 0.1 from surface to bottom. Furthermore, T_0 is the net sediment transport due to residual flow, and $T_{O1,K1}$, T_{M2}, T_{M4} are net transports related to O_1–K_1, M_2, and M_4 tidal pumping mechanisms, respectively. Component $T_{\eta u C_0}$ is the net sediment transport due to the correlation between the sea level variation and the tidal current, acting with mean SSC. Component $T_{\eta c U_0}$ is the net sediment transport due to the correlation between the tidal components of sea level variation and SSC, acting with the residual flow. Finally, $T_{\eta c u}$ is the net sediment transport

due to the triple correlation of tidal components of sea level variation, velocity, and SSC.

Due to the fact that the measurement for June 1999 only lasted for 14 h, a test was done to investigate how accurate the O_1–K_1 components are obtained from the 14 h. To address this point, we took the August 2008 data (which spans 25 h) and remained only the first 14 h. From this, new data set values of the O_1–K_1 components were computed. The results showed that the difference between this new data set (14 h) and the original data set (25 h) was around 20 %, which is considered to be acceptable in our study.

2.3 Deriving main components of residual flow

In order to identify the net sediment transport due to different residual flow components, a simple analytical model was used to derive residual flow components that are forced by individual physical mechanisms, involving river discharge, density-driven flow, Stokes return flow, tidal rectification, and asymmetry in mixing during the tidal cycle. The model resembles that used by Ianiello (1977), McCarthy (1993), and Cheng et al. (2010), but the bottom boundary condition is modified from no slip to partial slip. The difference with the model of Chernetsky et al. (2010) is that open boundary is used at the seaward and landward sides. The model assumptions and equation-solving techniques follow previous models. The model domain is a straight estuary channel that has constant depth and width, with cross-channel uniform conditions (Fig. 3).

In contrast to more sophisticated numerical models, the present model only yields an approximate description of the complex geometry and dynamics of the North Passage. Yet, it has a major advantage, viz. that it allows for systematic assessment of the contribution of residual flow components generated by different forcing agents to the total net sediment flux and net sediment transport. In this way, more fundamental insight into the complex dynamics of the system is obtained. The success of earlier models of this kind, which were cited above, motivates the application of this approach.
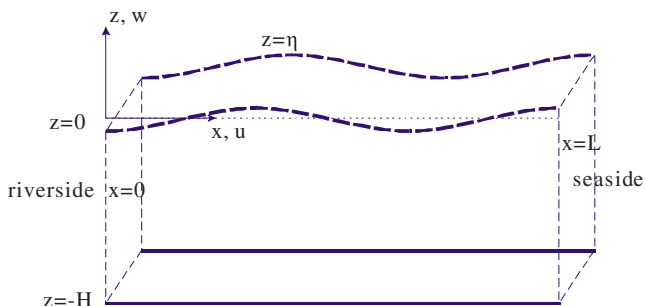

Fig. 3 Sketch of the model geometry. The *blue dashed lines* represent tidal elevations. Location $x=0$ corresponds to that of the reference point in Fig. 2

2.3.1 Governing equations

The flow in the along-channel direction is governed by the shallow water equation for cross-channel uniform conditions,

$$\frac{\partial u}{\partial t} + u\frac{\partial u}{\partial x} + w\frac{\partial u}{\partial z} = -g\frac{\partial \eta}{\partial x} + \frac{g}{\rho_0}\frac{d\rho}{dx}z + \frac{\partial}{\partial z}\left(A\frac{\partial u}{\partial z}\right), \quad (6a)$$

$$\frac{\partial u}{\partial x} + \frac{\partial w}{\partial z} = 0. \quad (6b)$$

Here, x (u) and z (w) denote the along-channel and vertical coordinates (velocity components), g is gravitational acceleration, and $\rho_0 \sim 1,020$ kg m^{-3} is the reference density. The along-channel density gradient is prescribed and denoted by dρ/dx. Furthermore, η is the location of the free surface, and A is the vertical eddy viscosity coefficient, which varies during the tidal cycle. Following Cheng et al. (2010), as a result of tidal straining, the vertical eddy viscosity coefficient can be written as

$$A = \overline{A} + A_1\cos(\sigma_2 t - \alpha), \quad (7)$$

where

$$A_1 = \overline{A}\left|\frac{d\rho}{dx}\right|\left(\frac{U}{\sigma_2\Delta\rho}\right).$$

Here, $\overline{A}$ is a constant, tidal mean eddy viscosity coefficient. Further, $A_1(<\overline{A})$ is the amplitude of the tidal varying part which depends on the horizontal density gradient and tidal flow amplitude, where $\Delta\rho$ is the typical density difference and U is the typical tidal velocity. Physically, A_1 is proportional to the tidal mean eddy viscosity coefficient $(\overline{A})$, density gradient over typical density difference (|dρ/dx|/$\Delta\rho$), and the typical length scale over which density gradient is advected (U/σ_2). Furthermore, α is a phase. Following Simpson et al. (1990) and Stacey et al. (2008), the strongest A occurs at the end of flood.

At the surface, it is assumed that the water motion is stress free and satisfies the kinematic boundary condition,

$$A\frac{\partial u}{\partial z} = 0, w = \frac{d\eta}{dt}, \text{at z} = \eta. \quad (8a)$$

At the bottom, a partial slip condition and impermeability of the bottom are imposed,

$$A\frac{\partial u}{\partial z} = su, w = 0, \text{at z} = -H. \quad (8b)$$

At the landward boundary, a net transport of water due to freshwater input (q, discharge per time per unit width) is

imposed. Integration of continuity Eq. 6b and application of boundary conditions (Eqs. 8a, 8b, 8c, 8d, and 8e) then imply constant residual water transport along the channel,

$$\overline{\int_{-H}^{\eta} u\, dz} = q, \quad \text{for all x.} \tag{8c}$$

Here, the overbar $\overline{\cdot}$ denotes a tidal average or mean.

Finally, semi-diurnal tidal sea level variations are imposed at both side boundaries with amplitude Z, frequency σ_2, and phase angle Ψ:

$$\eta_{M2}(0, t) = Z_0 \cos(\sigma_2 t - \psi_0), \tag{8d}$$

at x = 0 (landward boundary),

$$\eta_{M2}(L, t) = Z_L \cos(\sigma_2 t - \psi_L), \tag{8e}$$

at x = L (seaward boundary).

2.3.2 Perturbation analysis and analytical results

By performing a perturbation analysis similar to, e.g., Ianiello (1977), a reduced and consistent set of model equations is obtained. Application of scaling analysis on the equation terms reveals a parameter ε, the tidal amplitude-to-depth ratio, which measures the intensity of the nonlinear terms with respect to that of linear terms. It is assumed that the parameter ε is not negligible but much smaller than 1. By collecting terms with equal powers of ε, a leading order system of equations (ε^0 terms) and a first-order system of equations (ε^1 terms) are obtained. Higher-order systems are not considered.

The leading order system of equations governs the semi-diurnal tidal motion, and the equations are given by

$$\frac{\partial u_0}{\partial t} = -g \frac{\partial \eta_0}{\partial x} + \overline{A} \frac{\partial^2 u_0}{\partial z^2}, \tag{9a}$$

$$\frac{\partial u_0}{\partial x} + \frac{\partial w_0}{\partial z} = 0, \tag{9b}$$

where the subscript 0 represents leading order.

The boundary conditions at the free surface and at the bottom are given by

$$\frac{\partial u_0}{\partial z} = 0, \quad w_0 = \frac{d\eta_0}{dt}, \text{at } z = 0, \tag{10a}$$

$$\overline{A} \frac{\partial u_0}{\partial z} = s u_0, \quad w_0 = 0, \quad \text{at } z = -H. \tag{10b}$$

At the side boundaries, the system was forced by externally prescribed semi-diurnal tides

$$\eta_0(0, t) = Z_0 \cos(\sigma_2 t - \psi_0), \tag{10c}$$

at x = 0 (landward boundary),

$$\eta_0(L, t) = Z_L \cos(\sigma_2 t - \psi_L), \tag{10d}$$

at x = L (seaward boundary).

Analytical solutions for the tidal motion (Eqs. 9a, 9b, 10a, 10b, 10c, and 10d) are

$$\eta_0 = Re\left\{\widehat{\eta}(x) e^{-i\sigma_2 t}\right\}, \tag{11}$$

$$u_0 = Re\left\{\widehat{u}(x, z) e^{-i\sigma_2 t}\right\}, \tag{12}$$

where Re denotes the real part of a complex variable, and

$$\widehat{\eta} = \frac{Z_0 e^{i\psi_0} \sin[k_*(L - x)] + Z_L e^{i\psi_L} \sin(k_* x)}{\sin(k_* L)},$$

$$\widehat{u} = \frac{ig}{\sigma_2} \frac{d\widehat{\eta}}{dx} \left[\frac{\cosh(\mu z)}{\cosh(\mu H) + \frac{\mu}{s}\sinh(\mu H)} - 1 \right],$$

with

$$\frac{d\widehat{\eta}}{dx} = -k_* \frac{Z_0 e^{i\psi_0} \cos[k_*(L - x)] + Z_L e^{i\psi_L} \cos(k_* x)}{\sin(k_* L)},$$

$$\mu = \sqrt{\frac{\sigma_2}{2\overline{A}}}(1 - i),$$

$$k_* = \frac{\sigma_2}{\sqrt{gH}} \left[1 - \frac{\tanh(\mu H)}{\mu H} \frac{s}{s + \mu \tanh(\mu H)} \right]^{-\frac{1}{2}}.$$

The system governing the dynamics of the dominant part of the residual flow is obtained by considering the first-order system (which contains terms that are an order ε smaller than the dominant tidal terms) and averaging these equations over a tidal cycle. This procedure, which is discussed in detail by Ianiello (1977) and Cheng et al. (2010), results in

$$\underbrace{\overline{u_0 \frac{\partial u_0}{\partial x} + w_0 \frac{\partial u_0}{\partial z}}}_{t} = -g \underbrace{\frac{\overline{d\eta_1}}{dx} + \frac{g}{\rho}\frac{d\rho}{dx}z}_{d} + \overline{A}\frac{\overline{\partial^2 u_1}}{\partial z^2}$$
$$+ \underbrace{\overline{A_1 \cos(\sigma_2 t - \alpha)\frac{\partial^2 u_0}{\partial z^2}}}_{a}, \tag{13a}$$

$$\int_{-H}^{0} \overline{u_1}\, dz + \underbrace{\overline{\eta_0 u_0|_{z=0}}}_{s} = \underbrace{q}_{q}. \tag{13b}$$

In these expressions, the overbar $\overline{\cdot}$ denotes averaging over a tidal period. Besides, q is the freshwater discharge per unit

width and subscript 1 represent first order. Further, $\smile$ denotes the individual forcing terms.

The boundary conditions at the free surface and at the bottom are given by

$$\frac{\partial u_1}{\partial z} + \underbrace{\overline{\eta_0 \frac{\partial^2 u_0}{\partial z^2}}}_{b} = 0, \quad \text{at } z = 0, \tag{14a}$$

$$\overline{A} \frac{\partial u_1}{\partial z} = s u_1, \quad \text{at } z = -H. \tag{14b}$$

Eqs. 13a and 13b together with boundary conditions 14a and 14b describe the residual water motion in the estuary which is driven by the residual forcing terms that are river discharge (q), along-channel density gradient (d), Stokes return water transport which compensates for the Stokes drift, i.e., correlation between horizontal and vertical water motion (s), stress-free surface condition (b), nonlinear tidal momentum advection (t), and asymmetric tidal mixing (a). Since the equations are linear, the residual flow due to each forcing mechanism can be derived separately, i.e., the resulting solution for the along-channel residual flow u_1 and the sea surface elevation η_1 reads

$$\chi_1 = \chi_d + \chi_q + \chi_s + \chi_b + \chi_t + \chi_a, \tag{15}$$

where $\chi_1 = (u_1, \eta_1)$.

The analytical solution for the residual flow components are

$$u_d = -\frac{g}{48\overline{A}} \frac{1}{\rho} \frac{d\rho}{dx} \left[9\left(z^2 - H^2 - \frac{2\overline{A}H}{s} \right) \left(\frac{4\overline{A}H + sH^2}{3\overline{A} + sH} \right) + 8\left(z^3 - H^3 - \frac{3\overline{A}H^2}{s} \right) \right], \tag{16}$$

$$u_q = -\frac{q}{\frac{H^3}{3} + \frac{\overline{A}H^2}{s}} \left(\frac{z^2 - H^2}{2} - \frac{\overline{A}H}{s} \right), \tag{17}$$

$$u_s = \frac{\overline{\eta_0 u_0|_{z=0}}}{\frac{H^3}{3} + \frac{\overline{A}H^2}{s}} \left(\frac{z^2 - H^2}{2} - \frac{\overline{A}H}{s} \right), \tag{18}$$

$$u_b = -\overline{\eta_0 \frac{\partial^2 u_0}{\partial z^2}}\Big|_{z=0} \left[\frac{3}{4H} \left(\frac{2\overline{A} + sH}{3\overline{A} + sH} \right) \left(z^2 - H^2 - \frac{2\overline{A}H}{s} \right) + \left(z + H + \frac{\overline{A}}{s} \right) \right] \tag{19}$$

where

$$u_t = \left(\frac{\frac{z^2 - H^2}{2\overline{A}} - \frac{H}{s}}{\frac{H^3}{3\overline{A}} + \frac{H^2}{s}} \right) \left(\frac{1}{\overline{A}} \int_{-H}^{0} I(F_t)\, dz + \frac{H}{s} \int_{0}^{-H} F_t(x,z)\, dz \right) \tag{20}$$
$$+ \frac{I(F_t)}{\overline{A}} + \frac{\int_{0}^{-H} F_t(x,z)\, dz}{s},$$

$$I(F_t) = \overline{\int_{-H}^{z} \int_{0}^{z'} F_t(x, z'')\, dz''\, dz'}, \quad F_t(x,z) = \overline{u_0 \frac{\partial u_0}{\partial x}} + \overline{w_0 \frac{\partial u_0}{\partial z}}.$$

Finally,

$$u_a = \left(-\frac{\overline{A}}{2A_1} \right) \left(\left(\frac{\frac{z^2 - H^2}{2\overline{A}} - \frac{H}{s}}{\frac{H^3}{3\overline{A}} + \frac{H^2}{s}} \right) Re\left\{ \int_{-H}^{0} \widehat{u}\, dz \exp(-i\alpha) \right\} + Re\{ \widehat{u} \exp(-i\alpha) \} \right). \tag{21}$$

Here, salinity data are used to compute density gradient $d\rho/dx$, which is necessary to calculate flow components u_d in Eq. 16 and u_a in Eq. 21.

2.3.3 Estimation of values of density gradient, eddy viscosity, and slip number

The density gradient $d\rho/dx$ in Eqs. 16 and 21 was computed from salinity data S, assuming that density depends on salinity only, i.e., $\rho = \rho_0 + \beta S(x)$, where $\beta \sim 0.83$ kg m^{-3} psu^{-1} and S is the vertical mean salinity averaged over a tidal cycle in practical salinity unit. The values of tidal mean eddy viscosity $\overline{A}$ and slip number s were obtained by minimizing the difference between the observed and modeled M_2 tide current governed by the leading order system.

From the result of harmonic analysis on the field data, the M_2 tidal current can be written as

$$U_{M2}(x,z)\cos(\sigma_2 t - \varphi) = U_c \cos(\sigma_2 t) + U_s \sin(\sigma_2 t), \quad (22)$$

with $U_c = U_{M2}\cos(\varphi)$ and $U_s = U_{M2}\sin(\varphi)$. The modeled M_2 tidal current reads

$$u_0 = Re\{\hat{u}(x,z)e^{-i\sigma_2 t}\} = |\hat{u}|\cos(\sigma_2 t - \varphi')$$
$$= U_c'\cos(\sigma_2 t) + U_s'\sin(\sigma_2 t), \quad (23)$$

with $U_c' = |\hat{u}|\cos(\varphi')$, $U_s' = |\hat{u}|\sin(\varphi')$ and $\varphi' = \arg(\hat{u})$.

Thus, the expression for the difference between the observed and modeled M_2 tidal current is

$$G(\overline{A},\ s) = \sum_{i=1}^{n}\sum_{j=1}^{m}\Big[(U_c(i,j) - U_c'(i,j))^2 + (U_s(i,j) - U_s'(i,j))^2\Big], \quad (24)$$

with n being the number of stations and $m \sim 6$ the number of layers. By minimizing G with respect to $\overline{A}$ and s, the values of these parameters corresponding to the smallest difference are obtained. The relative error is also used to represent the performance of the model, which reads

$$RE = G / \sum_{i=1}^{n}\sum_{j=1}^{m}\Big(U_c(i,j)^2 + U_s(i,j)^2\Big). \quad (25)$$

3 Results

3.1 Field data

3.1.1 Tidal and seasonal behavior of SSC

Figure 4 shows the vertical distribution of currents and SSC at station CS3 during a tidal cycle prior to and after the DWP. The left panels show distributions in the wet seasons while right panels show distributions in the dry seasons. In the electronic supplement, the velocity and SSC data over the full measurement period are shown for three representative stations, i.e., CS2, CS3, and CS4. Salinity data are not shown, as this study focuses on flow and SSC dynamics. In all cases shown in Fig. 4, the SSC is small around slack water, and it reaches its maximum around peak flood and peak ebb, suggesting the resuspension of fine sediment from the bed by tidal currents. The peak SSC during ebb is much larger than that during flood, due to the facts that tidal current at peak ebb is larger than that at peak flood and the strong ebb tidal current lasts longer than flood tidal current. It turns out that the magnitude of local SSC is closely related to that of the tidal current. The sediment at the bed in the North Passage, which mainly consists of silt and clay with a median grain size of 7–16 μm (according to the samples taken during August 2008), with critical depth averaged erosion velocity of roughly 0.4–0.5 ms^{-1} (Li et al. 1998),

can be easily re-entrained. Thus, tidal currents play an important role in entrainment and transport of sediment.

The vertical distributions of SSC during wet season and dry season differ significantly. The distribution of the SSC during wet seasons is characterized by strong vertical gradients, while SSC is more vertically mixed during dry seasons. The reason is that the water during wet seasons (summer when the temperature is high) contains more organic matter, which triggers the flocculation of fine sediment (Xia and Eisma 1991) and these flocs rapidly settle.

The changes in the characteristics of the SSC cycle prior to and after the DWP involve three aspects. First, the peak bottom SSC doubled during wet seasons, while little change occurred during dry seasons, thus resulting in more significant seasonal cycle of the SSC after the DWP. Second, prior to the DWP, the vertical and time averaged SSC during flood or ebb in the wet season is much smaller than that in the dry season, while after the DWP, the averaged SSC during flood or ebb in the wet season is even larger than that in the dry season. Finally, during dry seasons, peak SSC occurred in the near bottom layer prior to the DWP, while after the DWP, it occurred in the bottom layer.

3.1.2 Longitudinal and vertical distribution of SSC

The ETM was well developed during both flood and ebb. The snapshots of longitudinal–vertical distribution of SSC at the time with maximal SSC during flood and ebb are shown in Fig. 5. The time corresponds to the hours indicated by black dotted lines in the velocity profiles of Fig. 4. The ETM was well developed at peak flood and peak ebb, or 1 h before or after those times. After the DWP, the turbidity maximum is more developed during wet seasons with larger peak SSC at the bottom.

In order to compare the location of the ETM prior to and after the DWP, the ETM zone is defined as the region where the near-bed SSC exceeds 2 kgm^{-3}. A 10–15-km upstream shift and extension of the ETM zone occurred after the DWP, and a new ETM core developed at station CS1 in the upper reach. During the wet season, the peak SSC near bed at ETM core increased from 6 to 15 kgm^{-3} with fluid mud forming around high water and early ebb in the middle reach, while there were minor changes in peak SSC during the dry season.

3.2 Flow components

3.2.1 Residual flow

The spatial distribution of the residual flow in the North Passage is shown in Fig. 6 for the wet and dry seasons prior to and after the DWP. Before the DWP, the residual flow structure in the lower reach was that of a gravitational

Fig. 4 Vertical profiles of
current velocity and SSC at
station CS3 during a tidal cycle.
Plus sign means seaward flow
and *minus sign* means landward
flow. *Left panels* display the
condition in wet seasons, while
right panels display the
condition in dry seasons. *Upper
two rows* display the condition
prior to the DWP, while *lower
two rows* display the condition
after the DWP. *Black dotted
lines* indicate the time when
estuarine turbidity maximum
was well developed in the
North Passage
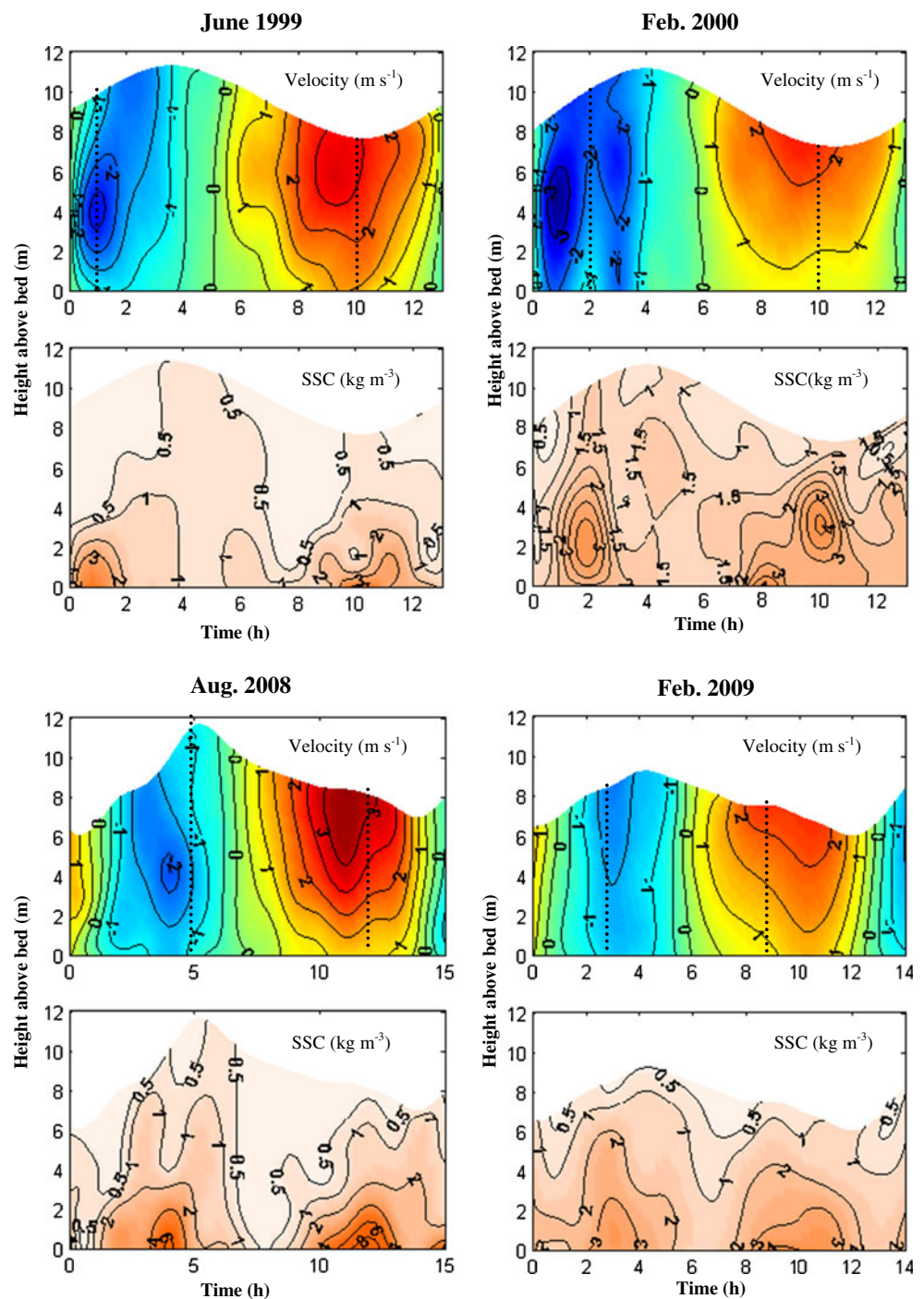
circulation in both wet and dry seasons, with inflow in the
lower layer and outflow in the upper layer. After the DWP,
in the wet season, the residual flow structure was signifi-
cantly modified, characterized by outflow throughout the
channel. In contrast, in the dry season, the residual flow
structure was still that of a gravitational circulation,
with an upstream shift of the zone of landward flow
near the bottom. Prior to the DWP, the seaward residual
flow was strong in the upper reach and decreased

seaward. After the DWP, the seaward residual flow
gradually increased from the upper reach to the middle
of the lower reach. In Fig. 2, the upper, middle, and
lower reaches are defined.

3.2.2 Tidal current components

Figure 7 shows the spatial distribution of the tidal current
components in the North Passage. It reveals that the tidal

Fig. 5 Longitudinal–vertical distribution of SSC (in kilograms per cubic meter) at the time when maxima SSC occurred during flood and ebb, corresponding to the hours with *black dotted lines* in the velocity profiles of Fig. 4. The *triangles* denote the location of measurement stations. *Left panels* display the distributions in wet seasons, while *right panels* display the distributions in dry seasons. *Upper two rows* display the distributions prior to the DWP, while *lower two rows* display the distributions after the DWP
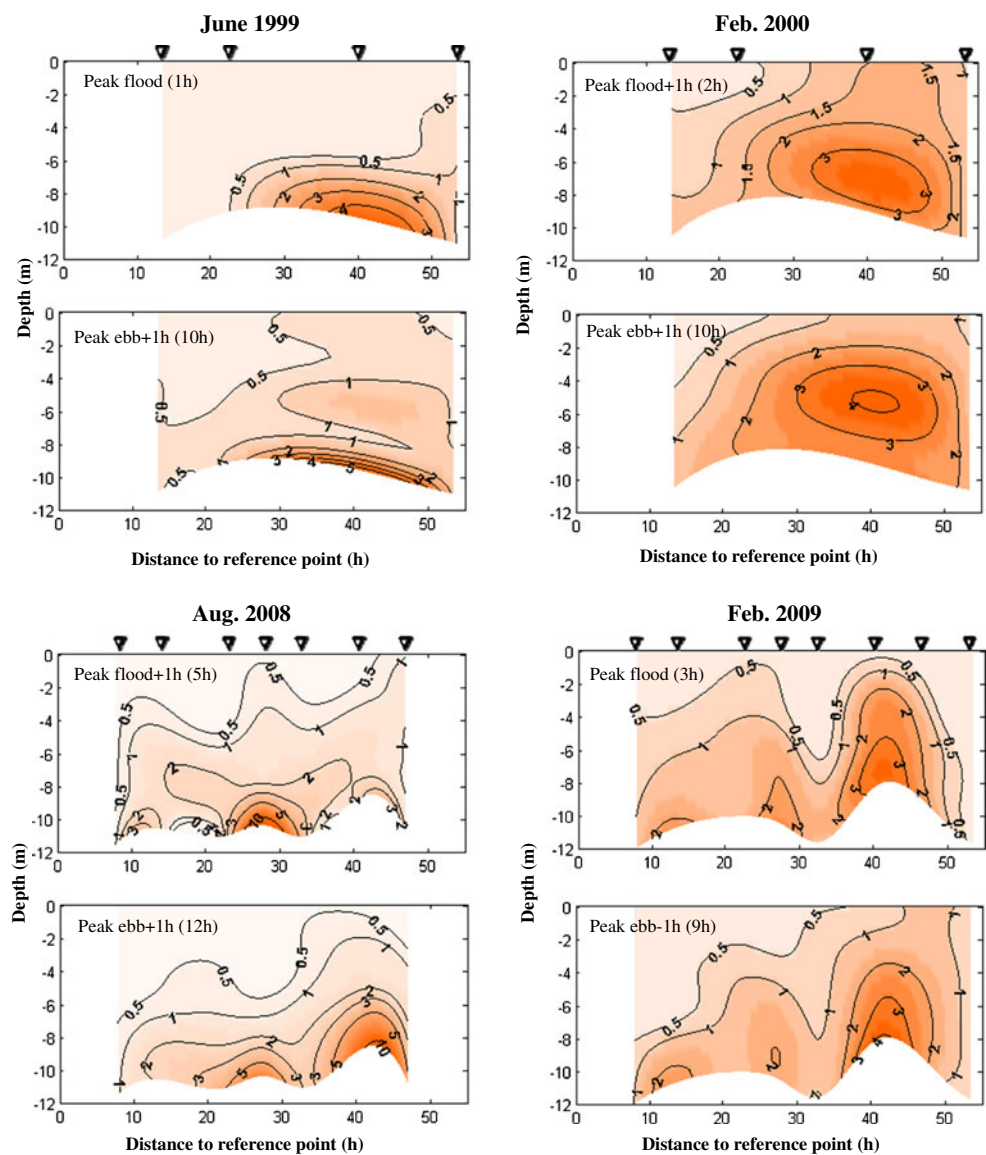
Fig. 6 Residual flow (in meters per second) structures in the North Passage. *Plus sign* means seaward flow and *minus sign* means landward flow. *Left panels* display the structures in wet seasons, while *right panels* display the structures in dry seasons. *Top row* displays the structures prior to the DWP, while *bottom row* displays the structures after the DWP
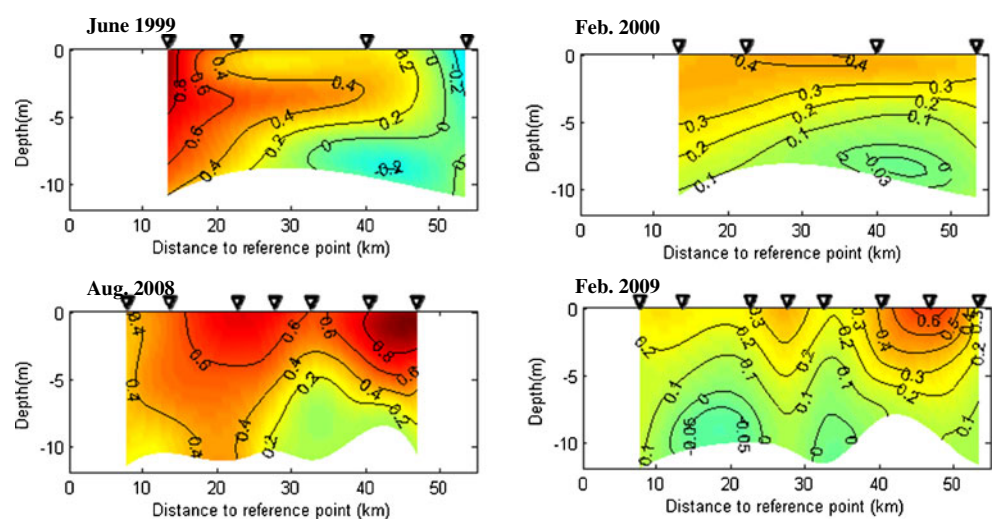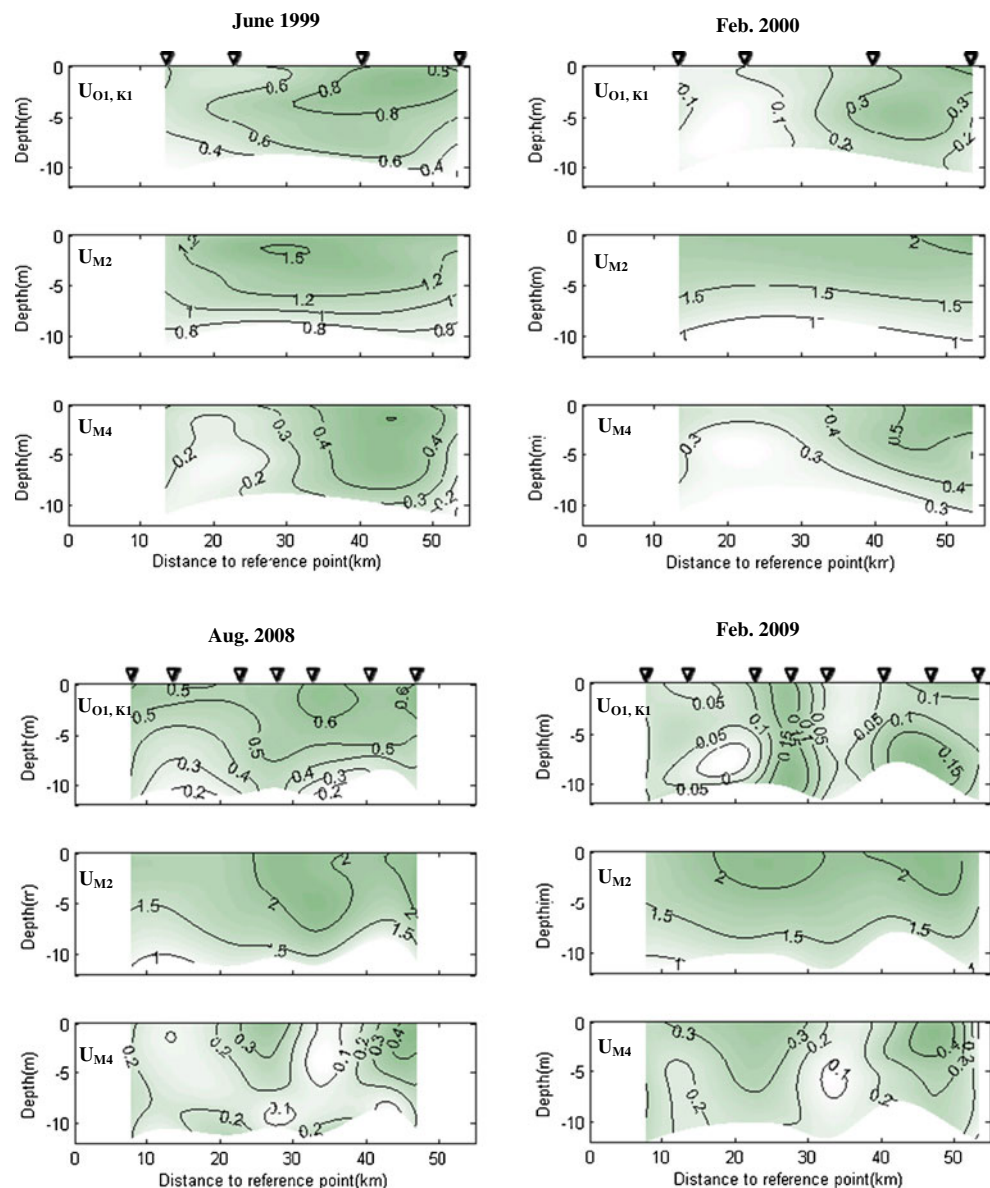
current was dominated by the M_2 constituent (U_{M2}),
followed by the components O_1–K_1 ($U_{O1,K1}$) and M_4
(U_{M4}), with maximum tidal velocities of 2.3, 0.9, and
0.5 ms^{-1}, respectively. Prior to the DWP, the tidal
current amplitudes slightly increased inland in the lower
reach and then gradually decreased. After the DWP,
they fluctuated considerably along the channel, indicat-
ing that the along-channel variation of the tidal dynam-
ics in the North Passage became more complicated due
to the engineering works. Overall, the amplitude of the
M_2 tidal current considerably increased due to the con-
verging of flow by training walls and groins. There was
a slight decrease in the amplitude of the O_1–K_1 tidal current,
while there was no significant change in the amplitude of M_4
tidal current.

3.3 Suspended sediment concentration components

3.3.1 Mean suspended sediment concentration

The pattern of the mean suspended sediment concentration,
denoted by C_0, is shown in the top panels in Fig. 8. During wet
seasons, the suspended sediment was trapped in the near bottom
layer, and it decreased sharply to the surface. After the DWP, the
peak bottom SSC increased from 2.5 to 5 kgm^{-3} in the wet season,
and the vertical mixing was slightly enhanced, leading to an overall
increase of the mean SSC in the entire channel. During dry
seasons, the suspended sediment was more vertically mixed. The
peak bottom SSC was around 2.3 kgm^{-3} both before and after the
DWP during dry seasons, but the vertical gradients of SSC in-
creased, resulting in a decrease in the SSC in the middle and upper

Fig. 8 Amplitudes of SSC components (in kilograms per cubic meter) in the North Passage. Here, C_0 is the mean concentration, $C_{O1,K1}$, C_{M2}, C_{M4} are the amplitudes of SSC components related to diurnal tide, semi-diurnal tide, and quarter-diurnal tide, respectively. *Left panels* display the distributions in wet seasons, while *right panels* display the distributions in dry seasons. *Upper four rows* display the distributions prior to the DWP, while *lower four rows* display the distributions after the DWP
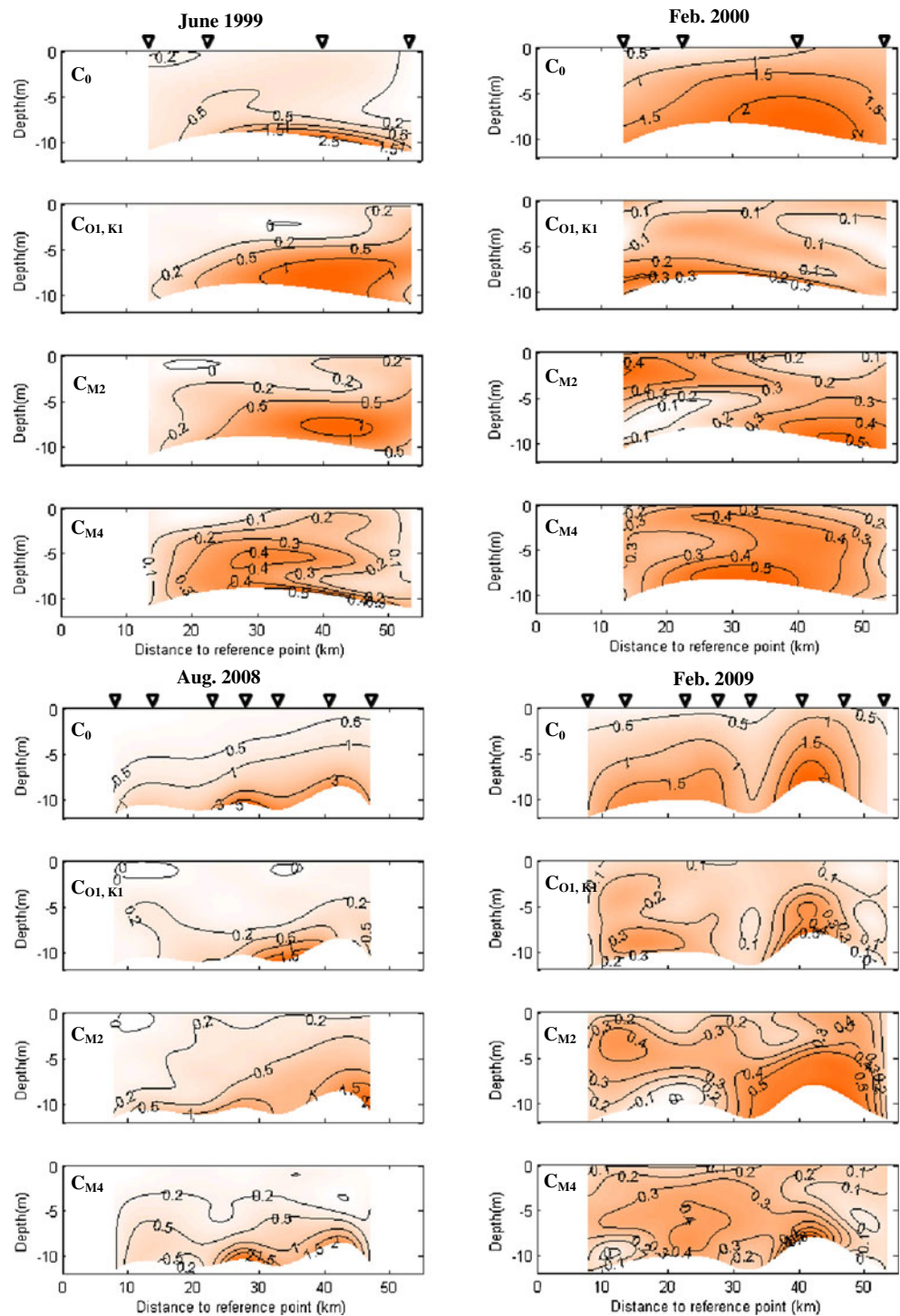
layers. The tidal mean SSC distribution during wet seasons after the DWP also shows an upstream extension and shift of the ETM.

3.3.2 Suspended sediment concentration components related to tides

The instantaneous SSC varied significantly during the tidal cycle in the North Passage, as shown by the distribution of amplitudes of SSC components related to tidal constituents O_1–K_1, M_2, M_4 in Fig. 8, denoted by $C_{O1,K1}$, C_{M2}, C_{M4}. During wet seasons, the peak SSC value of each tidal component reached almost half of the peak value of the mean SSC, except the M_4 component prior to the DWP. During dry seasons, the peak SSC value of each tidal component equaled 15–25 % of the peak value of the mean SSC prior to the DWP and 30 % of the peak value of the mean

SSC after the DWP. Amplitudes of tidal SSC components increased significantly after the DWP. During the wet season, the peak values of C_{M2} and $C_{O1,K1}$ doubled, and the peak value of C_{M4} even tripled. During the dry season, the peak value of $C_{O1,K1}$ doubled, and there was no significant change in C_{M2} and C_{M4}.

3.4 Net sediment flux and transport

3.4.1 Patterns of net sediment flux

The patterns of net sediment fluxes in the North Passage due to individual mechanisms, involving residual flow and various tidal pumping mechanisms, are presented in Fig. 9. The magnitudes of the net sediment fluxes reveal that residual flow and M_2 tidal pumping were dominant forcing agents in all cases. O_1–K_1 tidal pumping also had a large effect on sediment fluxes during the wet season prior to the DWP.

During the wet season prior to the DWP, the structure of the net sediment flux due to residual flow resembled that of the gravitational circulation, with seaward sediment flux landward of the null point (a place where the tidal and river flows meet and converge) and a two-layer sediment flux seaward of that point, leading to sediment trapping near the null point. The net sediment flux due to O_1–K_1 tidal pumping turned out to be divergent, but the seaward sediment flux in the lower reach was much stronger than landward sediment flux in the upper reach. The net sediment flux due to M_2 tidal pumping was convergent, causing sediment trapping near the point of convergence. The net sediment flux due to M_4 tidal pumping had a similar pattern as that of O_1–K_1 tidal pumping, albeit with a smaller magnitude. Overall, the net sediment flux was dominated by seaward directed components due to residual flow and M_2 tidal pumping in the upper reach and by landward directed components due to residual flow and M_2 tidal pumping in the lower reach. This resulted in sediment trapping in the middle and lower reach.

During the wet season after the DWP, the net sediment flux due to residual flow was directed seaward throughout the channel. The M_2 tidal pumping induced an overall landward net sediment flux, with local exceptions in the lower layer of the upper and lower reach. The other two tidal pumping mechanisms both resulted in divergence of net sediment flux, with local exceptions at the bottom, but their magnitudes were an order smaller than that of previous two fluxes. Thus, the total net sediment flux was dominated by a seaward directed component due to residual flow in the upper reach and a landward directed component due to M_2 tidal pumping in the middle reach, resulting in sediment trapping in the middle reach. Local sediment convergence due to various tidal pumping mechanisms caused weak sediment trapping in the upper reach.
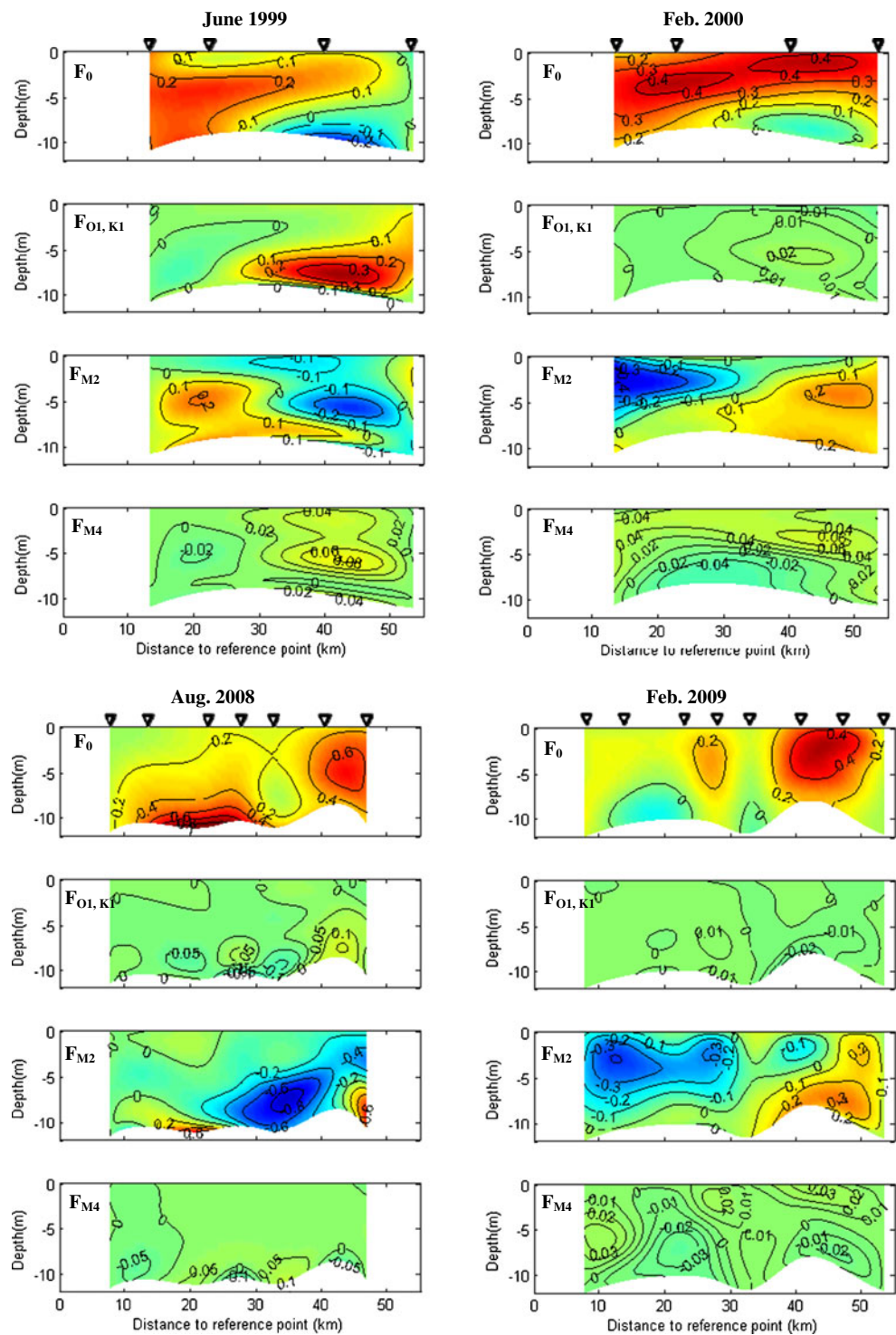
During the dry season prior to the DWP, the net sediment flux due to residual flow displayed the same distribution as that during the wet season. The net sediment flux due to M_2 tidal pumping had a divergent pattern. The net sediment flux due to M_4 tidal pumping was directed landward in the lower layer and seaward in the upper layer with small magnitudes. The divergent net sediment flux due to O_1–K_1 tidal pumping was negligible. Therefore, the total net sediment flux was dominated by components due to residual flow and M_2 tidal pumping, which opposed each other in the upper reach and lower layer of the lower reach, but were both seaward directed in other areas. Trapping of sediment at the bottom resulted from fluxes due to the residual flow and M_4 tidal pumping.

During the dry season after the DWP, the general structures of net sediment flux due to residual flow and M_2 tidal pumping did not change. However, the zone with landward sediment flux induced by residual flow in the lower layer shifted landward and separated into two parts, one in the upper reach and the other in the middle reach. In the upper and middle reach, the seaward sediment flux due to residual flow significantly decreased, while the area with landward sediment flux due to M_2 tidal pumping had a downward extension. Thus, in the upper and middle reach, the total net sediment flux was dominated by landward directed sediment flux due to M_2 tidal pumping, and it was enhanced by the landward directed flux due to residual flow at the lower layer, leading to trapping of sediment in this reach.

3.4.2 Net sediment transport

Net sediment transports induced by individual physical mechanisms and the total net sediment transport in the main channel of the North Passages are shown in Fig. 10. Besides the net transports generated by the residual flow (T_0) and various tidal pumping mechanisms ($T_{O1,K1}$, T_{M2}, T_{M4}), due to the triple correlations of sea level variation, currents, and SSC, three other transport terms arise, which are the transport $T_{\eta u C_0}$ as a consequence of the correlation between horizontal and vertical water motion acting with the mean SSC, the transport $T_{\eta c U_0}$ due to the correlation between tides and tidal components of SSC acting with residual flow, and the transport $T_{\eta c u}$ due to the triple correlation of tidal components of sea level variation, velocity, and SSC. These three transport terms measure the contribution of sea level variations to the net sediment transport. The term $T_{\eta u C_0}$ produced strong landward sediment transport, especially during dry seasons, thereby contributing to sediment trapping. Hereafter, this term is called the Stokes transport. The term $T_{\eta u c}$ also induced landward sediment transport but with a much smaller magnitude whose maximum is around 0.3 $\mathrm{kg\,m^{-1}\,s^{-1}}$. The magnitude of $T_{\eta c U_0}$ is in order of 0.01 $\mathrm{kg\,m^{-1}\,s^{-1}}$, with maximum of around 0.05 $\mathrm{kg\,m^{-1}\,s^{-1}}$ in all cases, which is negligible.

Fig. 9 Spatial structures of residual sediment fluxes (in kilograms per square meter per second) due to individual forcings in the North Passage. *Plus sign* means seaward flux and *minus sign* means landward flux. Here, F_0 is the residual sediment flux due to residual flow, and $F_{O1,K}$, F_{M2}, F_{M4} are fluxes due to tidal pumping mechanisms related to diurnal tide, semi-diurnal tide, and quarter-diurnal tide, respectively. *Left panels* display the structures in wet seasons, while *right panels* display the structures in dry seasons. *Upper four rows* display the structures prior to the DWP, while *lower four rows* display the structures after the DWP

During the wet season prior to the DWP, net sediment transport was dominated by seaward directed components due to residual flow, O_1–K_1 tidal pumping and M_4 tidal pumping, a landward Stokes transport, and a transport due to M_2 tidal pumping that was seaward in the upper reach and landward in the lower reach. The net transport due to

residual flow significantly decreased seaward and changed into a weak landward transport at station CS4. Overall, the total net downstream sediment transport decreased seaward, suggesting accumulation of the riverine suspended sediment throughout the channel. During the wet season after the DWP, net sediment transport was mainly composed of a
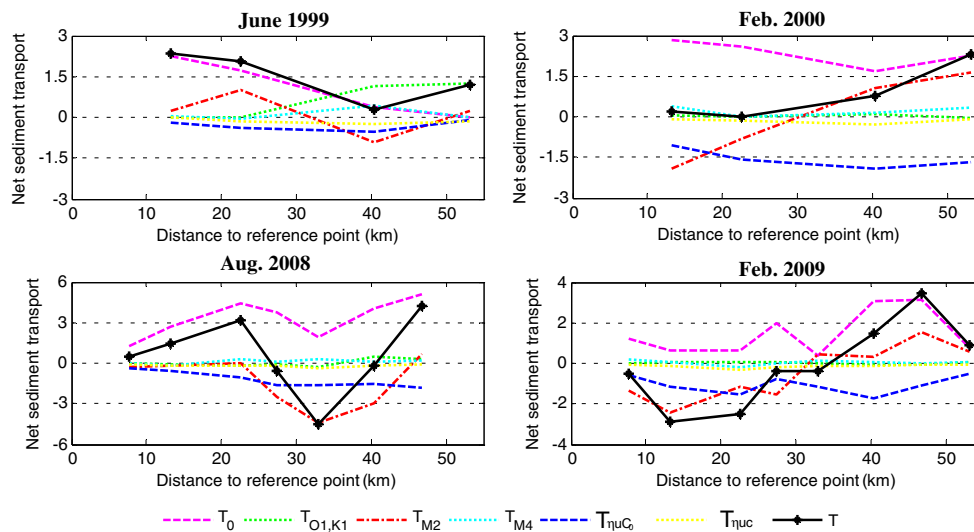
Fig. 10 Along-channel distribution of net sediment transport per unit width (in kilograms per meter per second) in the North Passage. *Plus sign* means seaward transport and *minus sign* means landward transport. Here, T_0 is the net sediment transport due to residual flow, $T_{\eta u C_0}$ is the Stokes transport, and $T_{\eta cu}$ is the net transport due to the triple correlation of tidal components of sea level variation, velocity, and SSC. Further, $T_{O1,K1}$, T_{M2}, and T_{M4} are net transports due to tidal pumping mechanisms related to diurnal tide, semi-diurnal tide, and quarter-diurnal tide, respectively, and T is the total net sediment transport. *Left panels* display the distributions in wet seasons, while *right panels* display the distributions in dry seasons. *Top row* displays the distributions prior to the DWP, while *bottom row* displays the distributions after the DWP

seaward directed component due to residual flow and landward directed components due to M_2 tidal pumping and Stokes transport. The total sediment transport was convergent, indicating sediment accumulation in the middle reach.

During the dry season prior to the DWP, net sediment transport was dominated by a seaward directed component due to residual flow, a landward Stokes transport, and a divergent transport due to M_2 tidal pumping that was directed landward in the upper reach and directed seaward in the lower reach. The total net downstream sediment transport gradually increased seaward in the middle and lower reach, indicating erosion of the river bed in that reach. During the dry season after the DWP, net sediment transport was also dominated by a seaward directed component due to residual flow, a landward Stokes transport, and a divergent transport due to M_2 tidal pumping which was directed landward in the upper reach and directed seaward in the lower reach. The total net sediment transport was divergent, indicating sediment entrainment in the upper and middle reach (CS1–CS7). However, the net landward sediment transport decreased inland at the entrance (CS1–CS0) and the net seaward sediment transport decreased seaward in the lower reach (CS7–CS4); hence, sediment accumulation occurred in these reaches.

Thus, the significant changes occurred in the net sediment transport components due to residual flow and M_2 tidal pumping prior to and after the DWP. The seaward net transport due to residual flow significantly decreased in the upper reach but increased in the lower reach. Consequently, the seaward decreasing net transport changed into seaward increasing transport. During wet seasons, the magnitudes of the main net

sediment transport components almost doubled, and net sediment transport due to M_2 tidal pumping changed, from being seaward in the upper reach and landward in the lower reach to being landward almost in the entire domain.

3.5 Main residual components and their sediment transport

Since the residual flow and the net sediment transport it induces have been greatly modified by the DWP, it is important to clarify and identify the main causes for these changes. For this, the changes that occurred in the main residual flow components and their sediment transport is discussed, which are forced by density gradient, river discharge, net tidal mass transport, tidal rectification, and asymmetry in tidal mixing. These residual flow components were derived by the analytical model presented in Section 2.2, and the values of eddy viscosity and slip number used are shown in Table 2. The comparison between the observed and modeled M_2 tidal current is presented in

Table 2 Vertical eddy viscosity coefficient and slip parameter

Time	Vertical eddy viscosity coefficient ($\bar{A}$, $m^2 s^{-1}$)	Slip parameter (s, ms^{-1})	Value of G (ms^{-1})	Relative error (%)
June 1999	0.003	0.004	0.11	17.5
February 2000	0.004	0.004	0.25	25.3
August 2008	0.0045	0.004	0.13	15.1
February 2009	0.006	0.004	0.20	19.8

Fig. 11. Besides, the value of absolute error (G in Eq. 24) and relative error (RE in Eq. 25) are presented in Table 2 to show the performance of the model. It turns out that the relative error is about 15–25 %, so the model performance is satisfactory, considering the aims for which it has been designed, i.e., gaining fundamental insight. The structures of residual flow components are presented in Figs. 12 and 13, and net sediment fluxes that they induced are presented in Figs. 14 and 15. The net sediment transports caused by individual agents are shown in Fig. 16. Since the magnitude of residual component due to stress-free surface condition is much smaller than that of other components, it is not discussed here.

Fig. 11 The comparison between the observed and modeled amplitude of M_2 tidal velocity and phase difference between the semi-diurnal horizontal and vertical tide. The dashed lines represent model predictions; the dots show measured data at various measuring locations. The left panels represent amplitude of M_2 tidal velocity along the estuary, and the red and blue colors represent the predicted and measured velocity at the surface and vertical mean velocity, respectively. The right panels depict relative phase shift between the free surface elevation and vertical mean along-channel velocity component
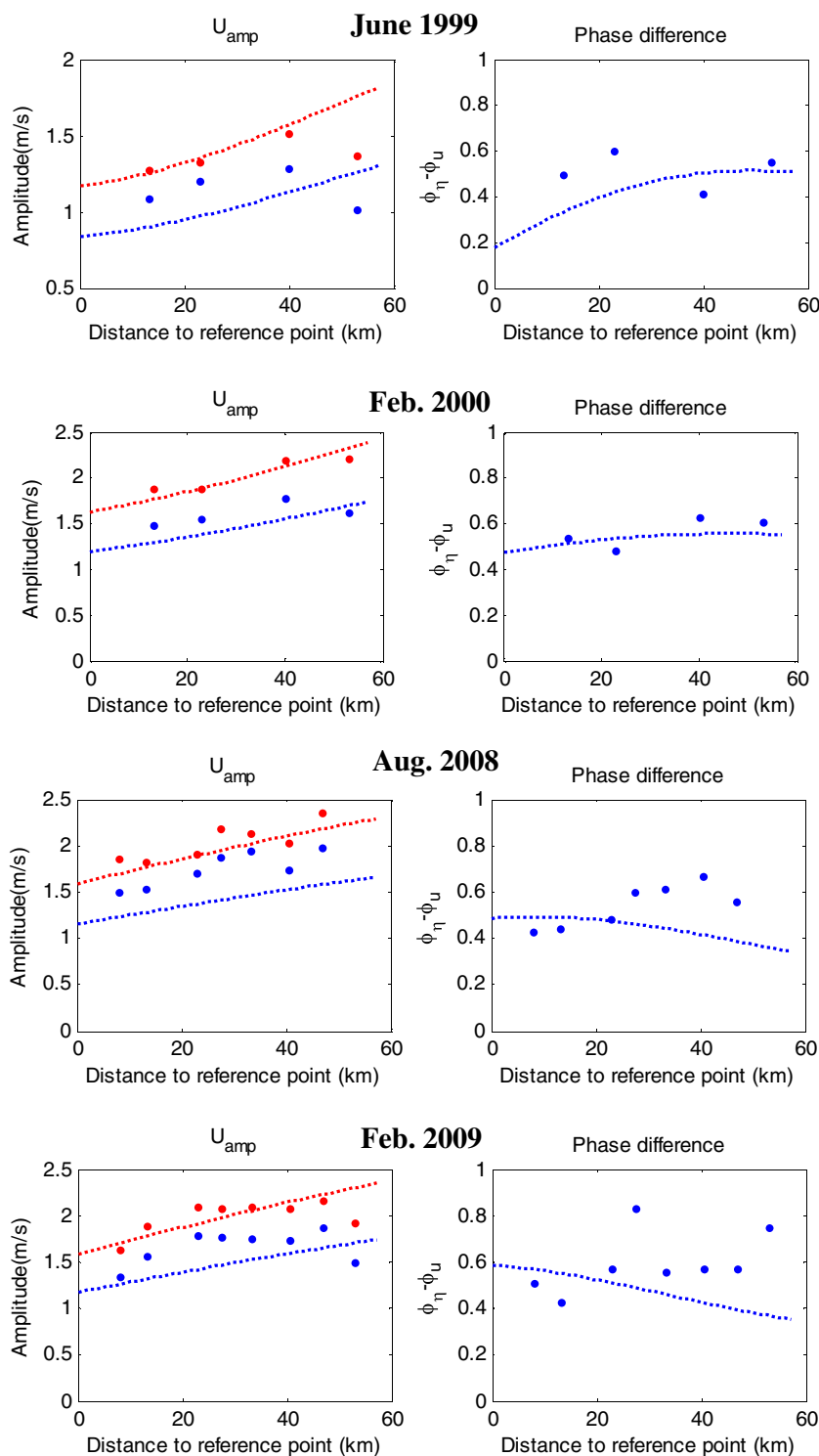
Fig 12 Residual flow components (in meters per second) due to individual forcings in the North Passage prior to the DWP. *Plus sign* means seaward flow and *minus sign* means landward flow. u_d, u_q, u_s, u_t, and u_a are residual flows due to density gradient, river discharge, Stokes return flow, tidal rectification, and asymmetry in tidal mixing, respectively. *Left panels* display the structures in wet seasons, while *right panels* display the structures in dry seasons
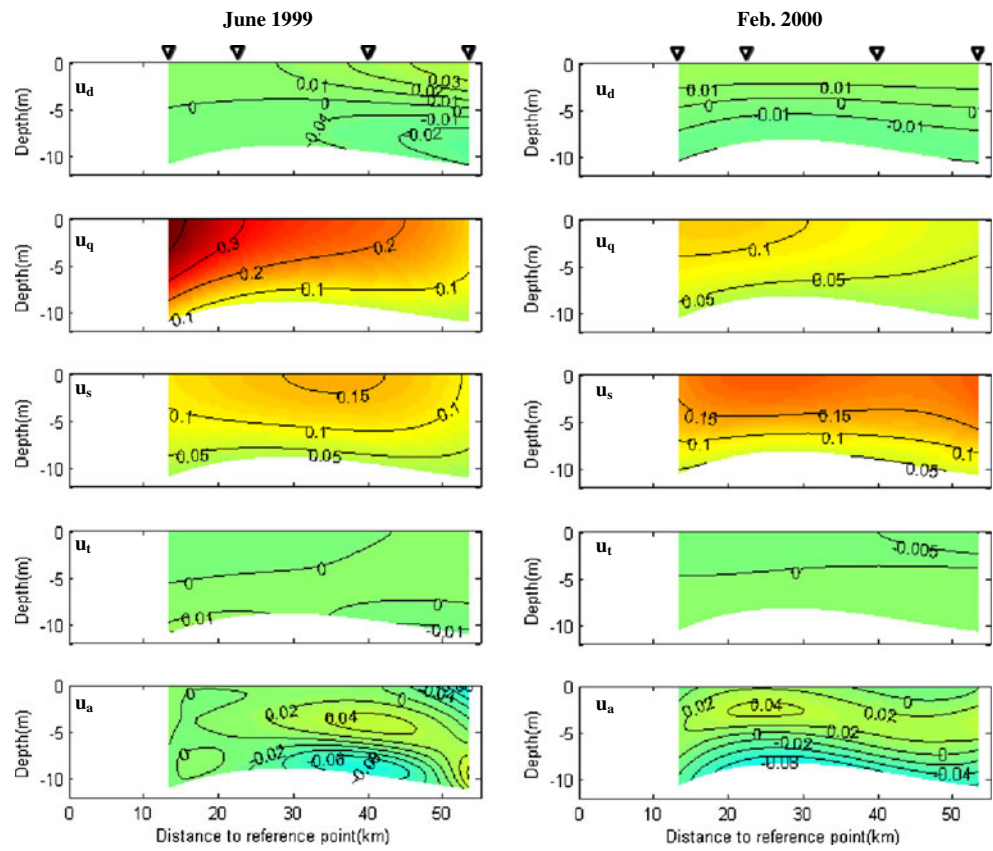

Fig 13 Residual flow components (in meters per second) due to individual forcings in the North Passage after the DWP. *Plus sign* means seaward flow and *minus sign* means landward flow. u_d, u_q, u_s, u_t, and u_a are residual flows due to density gradient, river discharge, Stokes return flow, tidal rectification, and asymmetry in tidal mixing, respectively. *Left panels* display the structures in wet seasons, while *right panels* display the structures in dry seasons. The salinity data were not obtained in February 2009, so two plots are missing in the *right panels*
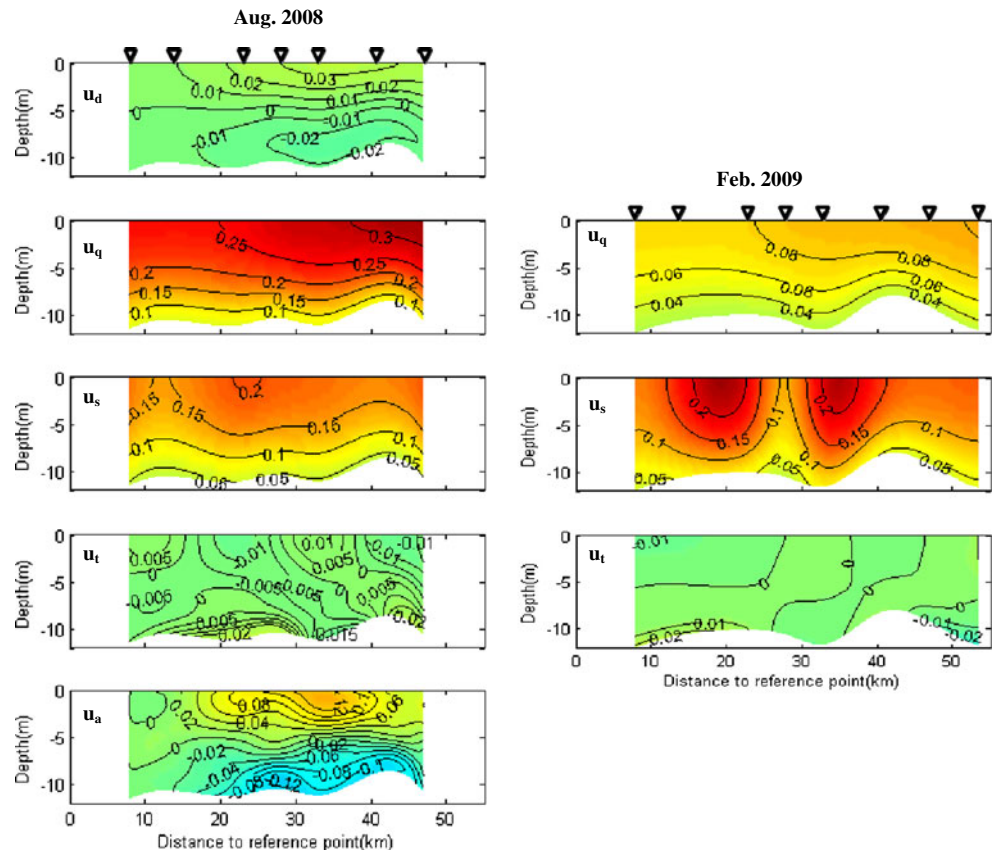
Fig. 14 Structure of residual sediment flux (kilograms per square meter per second) due to individual residual components in the North Passage prior to the DWP. *Plus sign* means seaward flux and *minus sign* means landward flux. F_d, F_q, F_s, F_t, and F_a are residual sediment fluxes due to density gradient, river discharge, Stokes return flow, tidal rectification, and asymmetry in tidal mixing, respectively. *Left panels* display the structures in wet seasons, while *right panels* display the structures in dry seasons
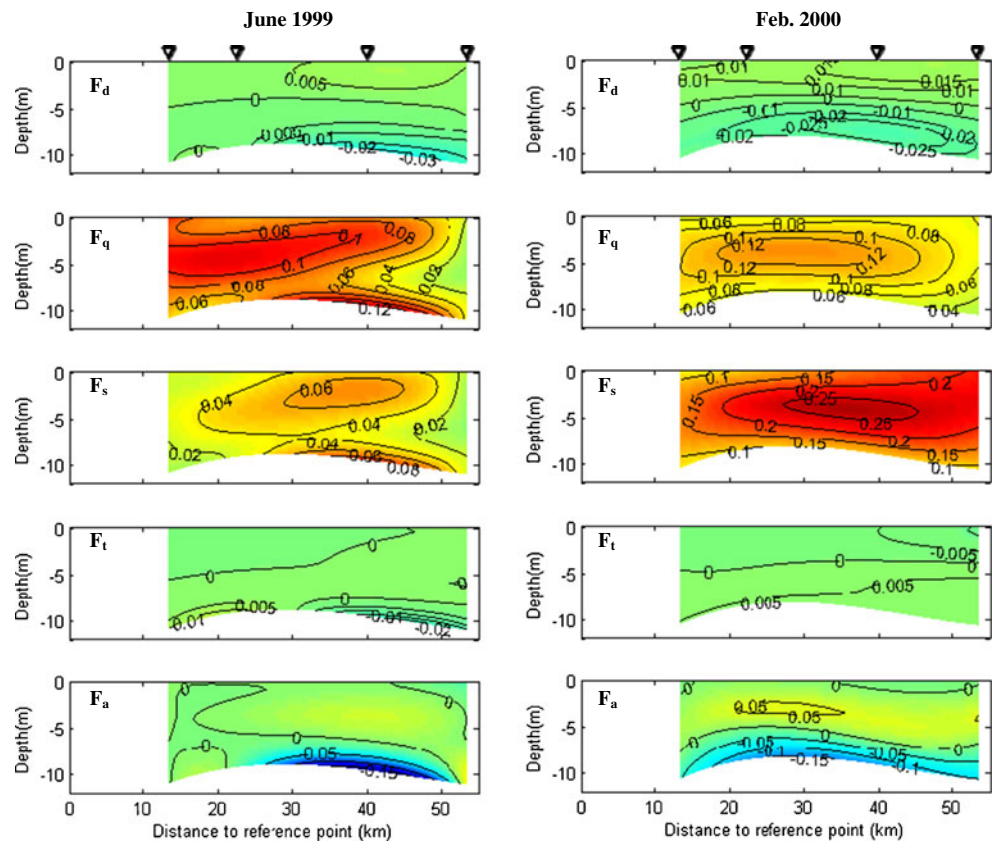

Fig. 15 Structure of residual sediment flux (kilograms per square meter per second) due to individual residual components in the North Passage after the DWP. *Plus sign* means seaward flux and *minus sign* means landward flux. F_d, F_q, F_s, F_t, and F_a are residual sediment fluxes due to density gradient, river discharge, Stokes return flow, tidal rectification, and asymmetry in tidal mixing, respectively. *Left panels* display the structures in wet seasons, while *right panels* display the structures in dry seasons
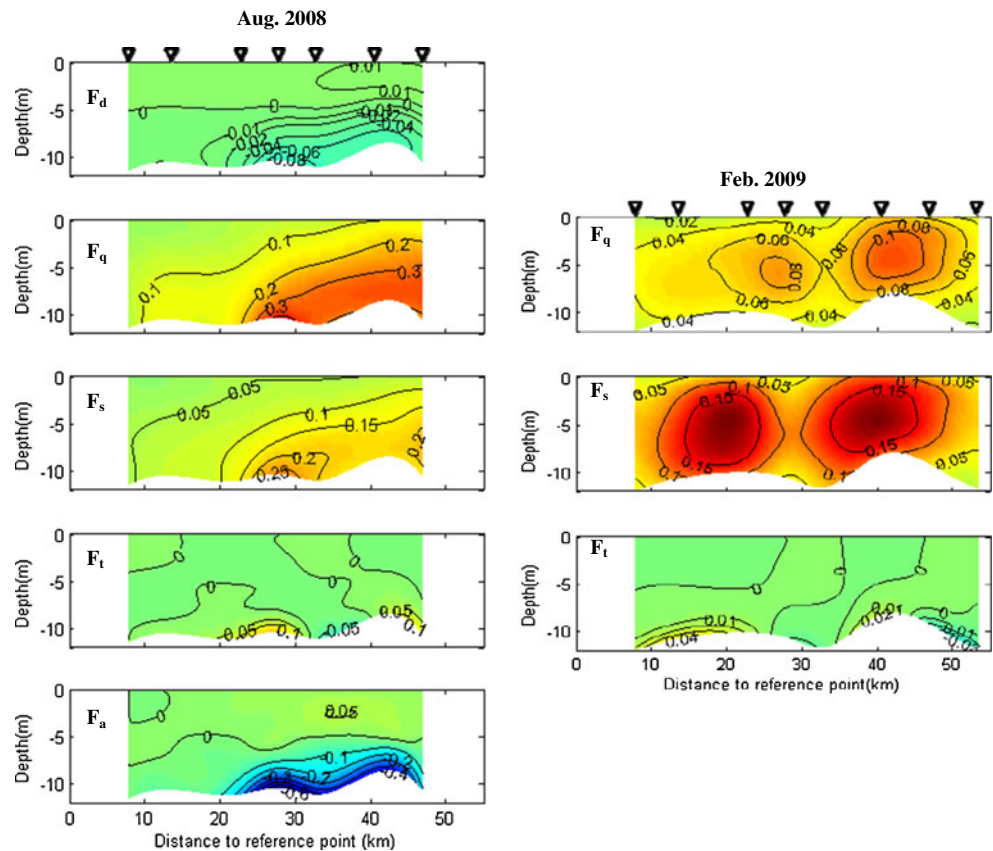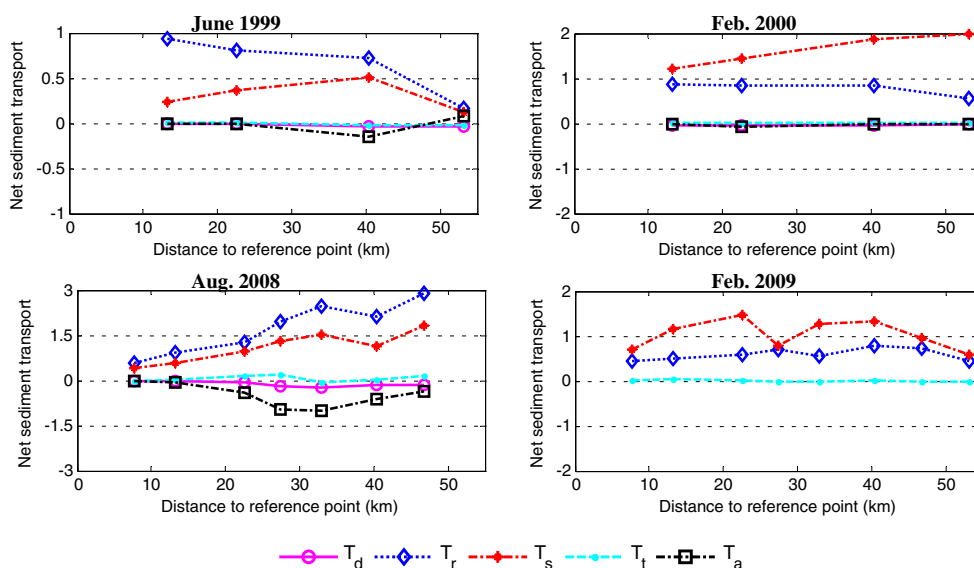
Fig. 16 Along-channel distribution of net sediment transport per unit width (kilograms per meter per second) in the North Passage due to main residual components. *Plus sign* means seaward transport and *minus sign* means landward transport. T_d, T_q, T_s, T_t, and T_a are sediment transports driven by density gradient, river discharge, Stokes return flow, tidal rectification, and asymmetry in tidal mixing, respectively. *Left panels* display the distributions in wet seasons, while *right panels* display the distributions in dry seasons. *Top row* displays the distributions prior to the DWP, while *bottom row* displays the distributions after the DWP

3.5.1 Density-driven flow

A gravitational circulation results from a balance between pressure gradient (caused by horizontal density gradients and surface slopes) and vertical mixing. Due to the fact that no salinity data were obtained in 2009, the density-driven flow and its sediment transport are missing at the top of the right lower panel of Figs. 12 and 13. The structure of the gravitational circulation did not change of course, with a landward flow at the lower layer and a seaward flow at the upper layer (u_d in Figs. 12 and 13). Note that the flow was rather week, consistent with what was found in other studies (cf. Chernetsky et al. 2010; Cheng et al. 2011). Nevertheless, during wet seasons, the location of maximum density gradient after the DWP had a slight upstream shift compared to that prior to the DWP. The landward net sediment flux in the lower layer is much stronger than that of the seaward sediment flux in the upper layer (F_d in Figs. 14 and 15). Thus, it caused a landward net sediment transport, but the magnitude of transport was small, smaller than $0.1\ \mathrm{kg\,m^{-1}\,s^{-1}}$ (Fig. 16).

3.5.2 River discharge

The residual flow induced by river discharge depends on the freshwater discharge at the landward side of the North Passage and the variation in the area of the cross section. Due to the frictional effects of the groins and the decrease in the volume of the North Passage, there was a significant decrease in the ebb flow diversion to the North Passage at

the bifurcation node of the South Channel (Jiang et al. 2012). Consequently, the freshwater input to the North Passage decreased, although the river discharge at the head of the estuary did not change much. The river discharge at the landward side of the North Passage decreased from 12,670 to 7,950 $\mathrm{m^3\,s^{-1}}$ in wet seasons (June 1999 to August 2008) and decreased from 3,324 to 2,485 $\mathrm{m^3\,s^{-1}}$ in dry seasons (February 2000 to February 2009).

Due to decreased river inflow at the entrance, u_q (Figs. 12 and 13) in the upper reach significantly decreased. Prior to the DWP, u_q gradually decreased seaward because of the discharging of flow into adjacent shoals and channels and expansion into an increased cross-sectional area. After the DWP, u_q gradually increased seaward in the middle and lower reach because the flow was concentrated in the main channel by training walls and groins, so u_q in the lower reach greatly increased compared to that prior to the DWP. The same change occurred in the net sediment transport due to river discharge (T_q in Fig. 16), but the change during dry seasons was not as significant as during wet seasons because the magnitude of the river discharge and its change prior to and after the DWP was much smaller.

3.5.3 Stokes return flow

The variation of the water surface and its correlation with tidal currents induces a net landward water transport. To balance this landward water transport, a seaward mean flow occurs, called Stokes return flow. Thus, Stokes return flow is a seaward residual flow, as is shown in Figs. 12 and 13

(u_s), and its strength is governed by the strength of the net water transport. During dry seasons, Stokes return flow dominated over river discharge. Prior to the DWP, the variation of u_s along the channel was minor, while after the DWP, it varied considerably along the channel, especially during the wet season, with one maximum in the upper reach and the other maximum in the middle reach. Overall, there was a 35 % increase in the magnitude of u_s after the DWP.

During wet seasons, prior to the DWP, the net sediment transport due to Stokes return flow (T_s in Fig. 16) increased seaward in the upper and middle reach and then decreased in the lower reach, while after the DWP, T_s generally increased seaward. During dry seasons, T_s dominated over T_q and became the most important transport term. Prior to the DWP, T_s generally increased seaward, while after the DWP, its along-channel variation was the same as that of u_s, with one maximum in the upper reach and the other maximum in the middle reach.

3.5.4 Tidal rectification

The nonlinear advection of along-channel tidal momentum, by both along-channel tidal flow and vertical tidal flow, results in a residual flow component, and the process is called tidal rectification. Here, due to the fact that only horizontal velocity was measured, only the advection of along-channel tidal momentum by along-channel tidal flow is considered. Prior to the DWP, the residual flow due to tidal rectification was rather week (u_t in Fig. 12). During the wet season, the pattern of u_t was convergent, contributing to sediment accumulation (F_t in Fig. 14). During the dry season, the pattern of u_t was opposite to that of the gravitational circulation, with outflow in the lower layer and inflow in the upper layer. However, the net sediment transport caused by tidal rectification is minor prior to the DWP (T_t in Fig. 16). After the DWP, the residual flow due to tidal rectification increased, especially during the dry season (u_t in Fig. 13). The structure of u_t and its sediment flux (F_t in Fig. 15) was generally convergent, with local divergence. The magnitude of net sediment transport due to tidal rectification (T_t) was still much smaller than that of river discharge and Stokes return flow.

3.5.5 Asymmetry in tidal mixing

As appears from Eq. 13a, the correlation between the time-varying eddy viscosity and the curvature of the M_2 tidal flow also results in a net flow. The physical origin of asymmetry in mixing is that straining of density by tidal flow leads to larger mixing during the flood (when salt water is advected over fresher water, thus causing an unstable density stratification) and weaker mixing during ebb (Simpson et al. 1990; Stacey et al. 2010; Burchard and Hetland 2010).

Following Cheng et al. (2010), we have modeled eddy viscosity such that it attains its largest value at the end of the flood tide. As shown in Figs. 12 and 13 (u_a), this results in a net flow with a pattern that is identical to that of density-driven flow (velocities are landward near the bottom and seaward near the surface), but with significantly larger magnitudes. These results are consistent with what is found both in data analysis (Stacey et al., 2010) and in numerical experiments (Burchard and Hetland 2010; Cheng et al. 2011). The flow u_a thus contributes to net landward transport of sediment, as shown in Fig. 16 (T_a).

Prior to the DWP, the residual flow due to asymmetric tidal mixing in the wet and dry seasons (u_a in Fig. 12) had a similar magnitude, which is five times larger than the value of the density-driven flow. However, with respect to the location of maximum landward flow in the bottom, there was a landward shift from the wet season to dry season. This is also the case for the location of maximum landward sediment flux in the bottom (F_a in Fig. 14).

After the DWP, in the wet season, u_a increased by nearly 40 %, with an upstream shift of the maximum landward flow. Thus, the net sediment transport due to asymmetric tidal mixing became a more significant contributor to the landward transport of sediment (see Fig. 16). For the wet season, u_a was not computed due to the lack of salinity data, but we would expect it to be important for the landward transport of sediment as well.

4 Discussion

The results presented in Section 3 show that the structure of residual flow in the North Passage, which is an important agent driving net sediment transport, has significantly changed. To identify the main causes leading to the change of the residual flow, main residual flow components were derived from an idealized model. Due to the fact that there were still residual flow mechanisms that might be important but not included in the model, such as net flow driven by lateral advection of along-channel momentum (cf. Lerczak and Geyer 2004, Huijts et al. 2009), there is still some difference between the observed residual flow and the sum of the five computed residual components. However, by comparing the change in the residual flow component due to river discharge and the change in the observed residual flow, it turns out that both of their magnitudes experienced a decrease in the upper reach, but an increase in the lower reach after the DWP. Thus, the changes that occurred in the residual flow due to river discharge are the main causes which led to the change in the structure of residual flow and its net sediment transport. The change in the structure of the residual flow in the flood seasons is mainly due to the increased u_q in the lower reach, while the upstream shift of

the seaward flow zone at the bottom in the dry seasons is mainly due to the decreased u_q in the upper reach.

The net sediment transport due to M_2 tidal pumping has also been greatly changed after the DWP during wet seasons. The main contributors to the M_2 tidal pumping are the tidal asymmetry, entering sediment dynamics through the bed shear stress due to presence of residual flow and M_4 tides, temporal and spatial settling lag, and asymmetry in tidal mixing. Thus, these different sources that contribute to M_2 tidal pumping are interesting to study in the near further to identify the main factors that caused the change in net sediment transport due to M_2 tidal pumping.

For the Yangtze Estuary, there is large amount of sediment input from the Yangtze River. Large part of these sediments was trapped in the bar area, where the North Passage is one of the channels intersecting the bar. Thus, large amounts of sediment were trapped in the North Passage. With respect to the sediment transport in the North Passage, the sediment accumulation occurs when the net seaward sediment transport decreases, so strong landward sediment transport is not necessary for the trapping of sediment.

In this paper, the measured changes in internal sediment transport processes (i.e., internal within the NP) were analyzed as a function of the unknown changes in external conditions, i.e., the changes in freshwater distribution and tidal movement in the estuary, affecting the water movement through the NP. These external changes in conditions led to changes in transport processes within the NP.

Finally, it is to be mentioned that the DWP were not the only modifications in the system. Morphological changes in the other channels of the Yangtze Estuary have affected the flow through the North Passage (Jiang et al. 2012). The construction of the Three Gorge Dam, which began to impound water in June of 2003 (Dai et al. 2011), induced the change in the riverine conditions, especially the decrease in sediment input from the Yangtze River. All these interventions had effects on the observed change in the flow structure and sediment transport in the NP. However, during the execution of the DWP, the significant change in flow, sediment transport, and subsequent morphological changes in the NP were mainly due to the DWP, as demonstrated by Jiang et al. (2012).

5 Conclusions

In this paper, the effects of the large-scale interventions on the flow structure, suspended sediment distribution, and its transport along the main channel of the North Passage of the Yangtze Estuary have been studied, with focus on explaining the changes in net sediment transport in terms of physical mechanisms. For this, field data in wet and dry seasons prior to and at the end phase of DWP were collected and analyzed by combining methods of harmonic analysis and results of an idealized model. From this, harmonic components of velocity and SSC as well as main residual flow components were obtained, and their roles in net sediment transport were assessed.

During the wet season prior to the DWP, the mean SSC distribution shows that sediment was trapped in the near bottom layer of the middle and lower reach. The net sediment transport components due to residual flow, Stokes transport, and M_2 tidal pumping were responsible for sediment trapping. Among the residual flow components, river discharge and Stokes return flow were the largest contributors to the residual flow and its net sediment transport.

During the wet season after the DWP, sediment was trapped in the lower layer of middle and lower reach. Compared to the situation prior to the DWP, the peak value of mean SSC doubled, and the ETM shifted upstream and extended. The increase in the mean SSC value was induced by the increase in the ebb tidal current velocity in the lower reach due to the engineering works and the increase in the fine sediment availability due to maintenance dredging, which caused stronger re-entrainment of sediment from the bed. The ETM shifted because of changes in net sediment transport components. Sediment trapping was mainly due to landward directed transport components due to M_2 tidal pumping and Stokes transport, as well as a seaward transport component due to residual flow. River discharge, Stokes return flow, and asymmetry in tidal mixing were the main contributors to the residual flow and its sediment transport, with the first two terms causing net seaward transport and the latter causing landward transport. The main reason for the upstream shift of the ETM was that the M_2 tidal pumping and residual flow due to asymmetric tidal mixing resulted in stronger landward transport components, while the upstream extension of the ETM was caused by the decrease in the seaward transport component due to residual flow in the upper reach, which is mainly due to the decrease in the river discharge there.

During the dry season prior to the DWP, the mean SSC also showed sediment accumulation in the middle and lower reach. The along-channel variation of the net sediment transport component due to residual flow (especially the flow due to river discharge) and the net sediment transport component due to Stokes transport were responsible for sediment trapping. Besides, residual flow component from asymmetric tidal mixing also contributed to sediment trapping by inducing a landward sediment transport. The sediment was more vertically mixed, and the zone of high SSC was more horizontally expanded compared to that in wet seasons, when sediment dynamics is strongly affected by flocculation processes.

During the dry season after the DWP, there was a slight upstream extension of the ETM, with minor decrease in the values of SSC compared to that prior to the DWP. Sediment trapping was mainly caused by net sediment transport components due to M_2 tidal pumping, Stokes transport, and

residual flow. Stokes return flow, river discharge, and tidal rectification were the main contributors to the residual flow and its net sediment transport. The reason for the upstream extension of the ETM was the same as that during wet seasons, but the extension in the dry season is minor compared to that in the wet season because the river discharge is overwhelmed by Stokes return flow among the seaward transport components in the dry season.

References

Burchard H, Hetland RD (2010) Quantifying the contributions of tidal straining and gravitational circulation to residual circulation in periodically stratified tidal estuaries. J Phys Oceanogr 40:1243–1262. doi:10.1175/2010JPO4270.1

Cheng P, Valle-Levinson A, de Swart HE (2010) Residual currents induced by asymmetric tidal mixing in weakly stratified narrow estuaries. J Phys Oceanogr 40:2135–2147

Cheng P, Valle-Levinson A, de Swart HE (2011) A numerical study of residual circulation induced by asymmetric tidal mixing in tidally dominated estuaries. J Geophys Res 116:C01017. doi:10.1029/2010JC006137

Chernetsky AS, Schuttelaars HM, Talke SA (2010) The effect of tidal asymmetry and temporal settling lag on sediment trapping in tidal estuaries. Ocean Dyn. doi:10.1007/s10236-010-0329-8

Cloern JE, Jassby AD (2012) Drivers of change in estuarine–coastal ecosystems: discoveries from four decades of study in San Francisco Bay. Rev Geophys. doi:10.1029/2012RG000397, 50, RG4001

Dai Z, Du J, Zhang X, Su N, Li J (2011) Variation of riverine material loads and environmental consequences on the Changjiang Estuary in recent decades. Environ Sci Technol 45:223–227

Dyer KR (1988) Fine sediment particle transport in estuaries. In: Dronkers J, van Leussen W (eds) Physical processes in estuaries. Springer, Berlin, pp 295–310

Dyer KR (1997) Estuaries: a physical introduction, seconded. Wiley, Chichester

Festa JF, Hansen DV (1978) Turbidity maxima in partially mixed estuaries: a two-dimensional numerical model. Est Coast Shelf Sci 7:347–359

Groen P (1967) On the residual transport of suspended matter by an alternating tidal current. Neth J Sea Res 3(4):564–574

Hansen DV, Rattray M (1965) Gravitational circulation in straits and estuaries. J Marine Res 23:104–122

Huijts KMH, Schuttelaars HM, de Swart HE, Friedrichs CT (2009) Analytical study of the transverse distribution of along-channel and transverse residual flows in tidal estuaries. Cont Shelf Res 29:89–100. doi:10.1016/j.csr.2007.09.007

Ianniello JP (1977) Tidally induced residual currents in estuaries of constant breadth and depth. J Mar Res 35:755–786

Jay DA, Musiak JD (1994) Particle trapping in estuarine tidal flows. J Geophys Res 99:445–461

Jiang C, Li J, de Swart HE (2012) Effects of navigational works on morphological changes in the bar area of the Yangtze Estuary. Geomorphology 139–140:205–219

Lerczak JA, Geyer WR (2004) Modeling the lateral circulation in straight, stratified estuaries. J Phys Oceanogr 34:1410–1429

Li J, Zhang C (1998) Sediment resuspension and implications for turbidity maximum in the Changjiang Estuary. Mar Geol 148:117–124

Liu G, Zhu J, Wang Y, Wu H, Wu J (2011) Tripod measured residual currents and sediment flux: impacts on the silting of the Deepwater Navigation Channel in the Changjiang Estuary. Est Coastal Shelf Sci. doi:10.1016/j.ecss.2010.08.008

McCarthy RK (1993) Residual currents in tidally dominated, well-mixed estuaries. Tellus 45A:325–340

North EW, Chao SY, Sanford LP, Hood RR (2004) The influence of wind and river pulses on an estuarine turbidity maximum: numerical studies and field observations in Chesapeake Bay. Estuaries 27:132–146

Officer CB (1981) Physical dynamics of estuarine suspended sediment. Mar Geol 40:1–14

Postma H (1967) Sediment transport and sedimentation in the estuarine environment. In: Lauff GH (ed) Estuaries. American Association of Advanced Science, Washington, DC, pp 158–179

Schuttelaars HM, de Swart HE (1996) An idealized long-term model of a tidal inlet. Eur J Mech B/Fluids 15:55–80

Shanghai Waterway Engineering Design and Consulting Co., Ltd. (2011) Research and technology program reports on the engineering measures to reduce the back-silting in the deep waterway of the North Passage of the Yangtze Estuary during the third phase of the Deep Waterway Project, pp 25–28 (in Chinese)

Simpson JH, Brown J, Matthews J, Allen G (1990) Tidal straining, density currents, and stirring in the control of estuarine stratification. Estuaries 13:125–132

Stacey MT, Brennan ML, Burau JR, Monismith SG (2010) The tidally averaged momentum balance in a partially and periodically stratified estuary. J Phys Oceanogr 40:2418–2434. doi:10.1175/2010JPO4389.1

Stacey MT, Fram JP, Chow FK (2008) Role of tidally periodic density stratification in the creation of estuarine subtidal circulation. J Geophys Res 113:C08016. doi:10.1029/2007JC004581

Talke SA, de Swart HE, Schuttelaars HM (2009) Feedback between residual circulation and sediment distribution in highly turbid estuaries: an analytical model. Cont Shelf Res 29:119–135. doi:10.1016/j.csr.2007.09.002

Uncles, RJ, Elliott RCA, Weston SA (1984) Lateral distributions of water, salt, and sediment transport in a partially mixed estuary. In: Proceedings of the 19th Coastal Engineering Conference, Houston, ASCE, Washington, DC, pp 3067–3077

Uncles RJ, Elliott RCA, Weston SA (1985) Observed fluxes of water, salt and suspended sediment in a partly mixed estuary. Estuar Coast Shelf S 20:147–167

Uncles RJ, Stephens JA, Harris C (2006) Runoff and tidal influences on the estuarine turbidity maximum of a highly turbid system: the upper Humber and Ouse Estuary. UK Mar Geo 235:213–228. doi:10.1016/j.margeo.2006.10.015

Winterwerp JC (2002) On the flocculation and settling velocity of estuarine mud. Cont Shelf Res 22:1339–1360

Xia FX, Eisma D (1991) Studies on the organic flocculation of suspended particles in the Changjiang Estuary. J East China Normal Univ (Natural Science) 1:66–70 (in Chinese, with English Abstr.)